Medler, K, Mazzali, PA, Teffs, J, Prentice, SJ, Ashall, C, Amenouche, M, Anderson, JP, Burke, J, Chen, TW, Galbany, L, Gromadzki, M, Gutierrez, CP, Hiramatsu, D, Howell, DA, Inserra, C, Kankare, E, McCully, C, Muller-Bravo, TE, Nicholl, M, Pellegrino, C and Sollerman, J

SN2020cpg: an energetic link between Type IIb and Ib supernovae

Monthly Notices of the ROYAL ASTRONOMICAL SOCIETY

MNRAS **506,** 1832–1849 (2021) https://doi.org/10.1093/mnras/stab1761
Advance Access publication 2021 June 22

SN 2020cpg: an energetic link between Type IIb and Ib supernovae

K. Medler [1]★ P. A. Mazzali,[1,2] J. Teffs [1] S. J. Prentice [3] C. Ashall [4] M. Amenouche,[5] J. P. Anderson,[6] J. Burke,[7,8] T. W. Chen,[9] L. Galbany [10] M. Gromadzki [11] C. P. Gutiérrez [12,13] D. Hiramatsu,[7,8] D. A. Howell,[7,8] C. Inserra [14] E. Kankare,[13] C. McCully,[7] T. E. Müller-Bravo [15] M. Nicholl,[16] C. Pellegrino[7,8] and J. Sollerman[9]

[1]*Astrophysical Research Institute Liverpool John Moores University, Liverpool L3 5RF, UK*
[2]*Max-Planck Institute for Astrophysics, Karl-Schwarzschild-Str. 1, D-85748 Garching, Germany*
[3]*Astrophysics Research Centre, School of Mathematics and Physics, Queen's University Belfast, Belfast BT7 1NN, UK*
[4]*Institute for Astronomy, University of Hawai'i at Manoa, 2680 Woodlawn Dr., Hawai'i, HI 96822, USA*
[5]*Université Clermont Auvergne, CNRS/IN2P3, LPC, Clermont-Ferrand, France*
[6]*European Southern Observatory, Alonso de Córdova 3107, Casilla 19, Santiago, Chile*
[7]*Las Cumbres Observatory Global Telescope Network, 6740 Cortona Dr. Suite 102, Goleta, CA 93117, USA*
[8]*Department of Physics, University of California, Santa Barbara 93106, USA*
[9]*The Oskar Klein Centre, Department of Astronomy, Stockholm University, AlbaNova, SE-10691 Stockholm, Sweden*
[10]*Departamento de Física Teórica y del Cosmos, Universidad de Granada, E-18071 Granada, Spain*
[11]*Astronomical Observatory, University of Warsaw, Al. Ujazdowskie 4, PL-00-478 Warszawa, Poland*
[12]*Finnish Centre for Astronomy with ESO (FINCA), FI-20014 University of Turku, Finland*
[13]*Tuorla Observatory, Department of Physics and Astronomy, FI-20014 University of Turku, Finland*
[14]*School of Physics & Astronomy, Cardiff University, Queens Buildings, The Parade, Cardiff, CF24 3AA, UK*
[15]*School of Physics and Astronomy, University of Southampton, Southampton, Hampshire, SO17 1BJ, UK*
[16]*Birmingham Institute for Gravitational Wave Astronomy and School of Physics and Astronomy, University of Birmingham, Birmingham B15 2TT, UK*

Accepted 2021 June 16. Received 2021 May 24; in original form 2021 March 17

ABSTRACT

Stripped-envelope supernovae (SE-SNe) show a wide variety of photometric and spectroscopic properties. This is due to the different potential formation channels and the stripping mechanism that allows for a large diversity within the progenitors outer envelope compositions. Here, the photometric and spectroscopic observations of SN 2020cpg covering ∼130 d from the explosion date are presented. SN 2020cpg ($z = 0.037$) is a bright SE-SNe with the B-band peaking at $M_B = -17.75 \pm 0.39$ mag and a maximum pseudo-bolometric luminosity of $L_{\rm max} = 6.03 \pm 0.01 \times 10^{42}$ erg s^{-1}. Spectroscopically, SN 2020cpg displays a weak high- and low-velocity H α feature during the photospheric phase of its evolution, suggesting that it contained a detached hydrogen envelope prior to explosion. From comparisons with spectral models, the mass of hydrogen within the outer envelope was constrained to be ∼0.1 M$_\odot$. From the pseudo-bolometric light curve of SN 2020cpg a ^{56}Ni mass of $M_{\rm Ni} \sim 0.27 \pm 0.08$ M$_\odot$ was determined using an Arnett-like model. The ejecta mass and kinetic energy of SN 2020cpg were determined using an alternative method that compares the light curve of SN 2020cpg and several modelled SE-SNe, resulting in an ejecta mass of $M_{\rm ejc} \sim 5.5 \pm 2.0$ M$_\odot$ and a kinetic energy of $E_{\rm K} \sim 9.0 \pm 3.0 \times 10^{51}$ erg. The ejected mass indicates a progenitor mass of 18−25 M$_\odot$. The use of the comparative light curve method provides an alternative process to the commonly used Arnett-like model to determine the physical properties of SE-SNe.

Key words: supernovae: general – supernovae: individual (SN 2020cpg).

1 INTRODUCTION

Core-collapse supernovae (CC-SNe) result from the death of stars with a Zero-Age Main Sequence (ZAMS) mass of $M_{\rm ZAMS} > 8$ M$_\odot$ (Woosley, Langer & Weaver 1995; Smartt 2009). These CC-SNe, separated into multiple categories based on their photometric and spectroscopic properties, are known as the H-rich Type II SNe (SNe II) and the H-poor stripped envelope SNe (SE-SNe). SNe II undergo little to no stripping of their outer hydrogen envelope prior to explosion and as such display strong hydrogen features throughout their spectral evolution. SE-SNe, however, lack the strong hydrogen features and display a variety of different spectroscopic properties depending on their elemental composition prior to core-collapse. The type of SE-SN can be determined by the presence and strength of both hydrogen and helium features within their spectra. These SNe include the H/He-rich Type IIb SNe (SNe IIb), the H-poor/He-rich Type Ib SNe (SNe Ib), and the H/He-poor Type Ic SNe (SNe Ic).

SNe Ib(c) lack any prominent hydrogen (and helium) spectral lines (Filippenko 1997), as their progenitor stars are thought to have been fully stripped of their outer hydrogen and H/He envelopes prior to the

★ E-mail: K.Medler@2019.ljmu.ac.uk

core-collapse event. The stripping of the outer envelopes for these progenitor stars is expected to occur over the last stages of the stars life cycle prior to core-collapse. The process required to strip the outer envelope from these massive stars is still under investigation. The predominant methods include binary interaction where mass is transferred to the companion star via Roche lobe overflow (e.g. Podsiadlowski, Joss & Hsu 1992; Stancliffe & Eldridge 2009; Soker 2017), and a single star formation channel where the outer envelope is stripped prior to collapse, during the Wolf–Rayet phase, by either stellar winds (e.g. Georgy et al. 2012; Gräfener & Vink 2015) or via rotational stripping (Groh, Meynet & Ekström 2013). Despite the existence of multiple potential formation channels for SE-SNe, the binary star model seems to be favoured in recent years as the dominant source of SE-SNe progenitors. This is because the single-star model is unable to produce the number of progenitors required to account for all the SE-SNe observed (Smith et al. 2011).

However, if the degree of stripping is not high enough to fully remove all of the hydrogen from the progenitor, a hydrogen envelope is present during the explosion resulting in a SNe IIb (see Woosley et al. 1994 for SN 1993J one of the best followed examples of SN IIb). SNe IIb are different to the other SE-SNe by the clear hydrogen features within their spectra that can persist for several months before slowly fading as the SN evolves into the nebular phase (see Filippenko 1997, 2000). Photometrically, SNe IIb are very similar to other SE-SNe displaying a main peak within the first two to three weeks from the explosion. Several SNe IIb also display a bright initial peak within a few days of the explosion prior to the main peak seen in all SE-SNe (see Bersten et al. 2012; Piro 2015). The initial luminous peak is thought to result from the shock cooling near the stellar surface (Waxman & Katz 2017), while the second main peak is a result of the radioactive decay of ^{56}Ni and ^{56}Co synthesized during the explosion. The dual peak light curve has been seen in several of the well observed SNe IIb, such as SN 1993J (Wheeler et al. 1993) and SN 2016gkg (Arcavi et al. 2017; Bersten et al. 2018), and also in some SNe Ib, such as SN 1999ex (Mazzali et al. 2002) and SN 2008D (Malesani et al. 2009). Although this feature is seen in both SNe IIb and Ib, it is not observed in the majority of SNe, because the progenitor compactness causes the shock to cool more quickly than surveys can observe the shock breakout. However, thanks to the improving cadence of present surveys, the probability of covering and detecting this feature will increase.

Spectroscopically SNe IIb differentiate themselves from SNe Ib by the presence of the hydrogen features which fade over time as the spectra of SNe IIb become more Ib-like, with the helium features becoming dominant. From detailed modelling of H-rich and H-poor SNe the mass of hydrogen within the outer envelope, $M_{\rm H}$, required to form a SNe IIb has been found to be within the range of $0.01-1.0\,{\rm M}_{\odot}$ (Sravan, Marchant & Kalogera 2019). Hachinger et al. (2012) constructed a detailed set of spectral models to determine the amount of hydrogen and helium that can be hidden within the outer envelope of SNe Ib/c, respectively. From their synthetic spectra, Hachinger et al. (2012) concluded that as little as 0.025–0.033 $\rm M_{\odot}$ is required to form a strong H α absorption feature, suggesting that some Type Ib's may display H α features further blending the distinction between IIb and Ib SE-SNe. More recently, Prentice & Mazzali (2017) showed that the distinction between the He-rich SE-SNe can be further blurred based on the strength of H α emission within the spectra. Prentice & Mazzali (2017) created two further SE-SNe subcategories; the Type IIb(I), which display moderate H-rich spectra where the H α P-Cygni profile is dominated by the absorption component relative to the emission profile, and the Ib(II), whose spectra only show some weak H α with no obvious Balmar lines more energetic than H α. The classification scheme of Prentice & Mazzali (2017) along with the findings of Hachinger et al. (2012) demonstrates that SNe IIb and Ib are likely more related than previously thought.

Here, we present the photometric and spectroscopic evolution for SN 2020cpg, a Type Ib SN with a thin hydrogen layer, during the first ∼130 d. SN 2020cpg was initially classified with the Supernova Identification code SNID (Blondin & Tonry 2007) as a Type Ib SN, from the spectrum obtained on 19/02/2020 with the Liverpool Telescope (LT; Steele et al. 2004). However, follow-up spectral observations suggest that SN 2020cpg displayed H α features as seen in Type IIb SNe. In Section 2.2, we present the *BgVri*-band photometry for SN 2020cpg from the first 130 d after the explosion obtained through various Las Cumbres Observatory Global Telescope network telescopes (LCO; Brown et al. 2013), as part of the Global Supernova Project (GSP; Howell & Global Supernova Project 2017). The spectroscopic observation of SN 2020cpg are presented in Section 2.3. In Section 3, we discuss the construction of the pseudo-bolometric light curve and the Arnett-like model used to obtain the physical parameters. In Section 4, we present the light curves for the *BgVri*-band photometry and the constructed pseudo-bolometric light curve, along with physical properties obtained by an Arnett-like model. In Section 4.3, we obtain the line velocity evolution, along with a comparison of SN 2020cpg spectra with other well followed Type Ib and IIb SNe. In Section 5, we discuss the potential presence of a hydrogen envelope and the spectral modelling done to determine its presence. We also discuss the use of hydrodynamical models to obtain more realistic explosion parameters and compare the results with those produced by the Arnett-like model. Finally, in Section 6, we summarize the finding on SN 2020cpg, giving final estimates for the physical parameters and a value of the progenitors initial mass.

2 OBSERVATIONS AND DATA REDUCTION

2.1 Explosion date and host galaxy

SN 2020cpg was first detected on 15/02/2020 (MJD = 58894.54) by Nordin et al. (2020) on behalf of the Zwicky Transient Facility (ZTF; Bellm et al. 2019). The last non-detection of SN 2020cpg, on 06/02/2020 (MJD = 58885.52), predates the ZTF discovery by 9 d. To place a better constraint on the explosion date of SN 2020cpg, we modified the pseudo-bolometric light curve model to include the explosion date as a parameter (see Section 3.2). From this fit, we obtain an explosion date of 08/02/20, MJD = 58887.7 ± 2.1 d, which we adopt throughout the rest of the paper. SN 2020cpg was associated with the galaxy SDSS J135219.64 + 133432.9 and was located 1.14 arcsec south and 24.07 arcsec west from the galaxy centre, just off the outer end of the host galaxy's western spiral arm, as seen in Fig. 1. Using the cosmological parameters of $\rm H_0 = 73.0 \pm 5.0\,km\,s^{-1}\,Mpc^{-1}$, $\Omega_{\rm matter} = 0.27$ and $\Omega_{\rm vacuum} = 0.73$ gives a redshift distance of 158.6 ± 11.1 Mpc, with the distance calculation based on the local velocity field model from Mould et al. (2000). The host redshift of $z = 0.037$ implies a distance modulus of $m - M = 36.05 \pm 0.15$ mag.

2.2 Photometry

The initial *g*- and *r*-band photometry was obtained by ZTF, using the ZTF-cam mounted on the Palomar 1.2m Samuel Oschin telescope several days (t[MJD] ≈ 58894.5) before continuous follow-up occurred. This photometry was run through the automated ZTF pipeline (Masci et al. 2019) and is presented on Lasair transient

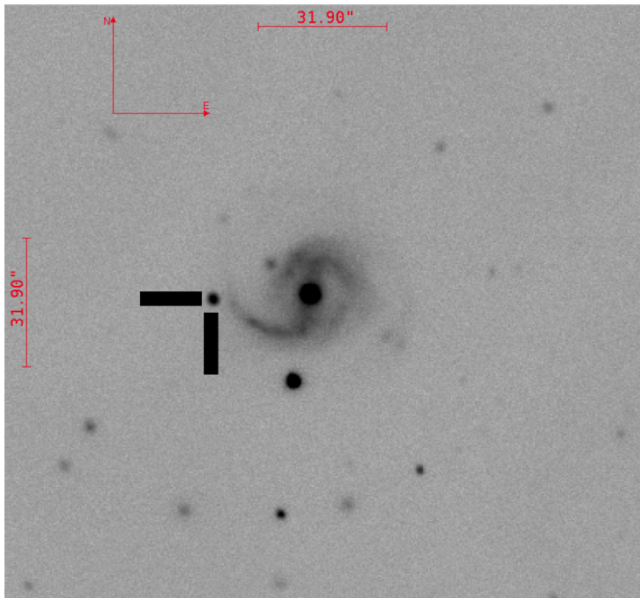

Figure 1. Image of SN 2020cpg and the host galaxy, obtained by combining LCO observations in *BgVri* filters on 20/02/2020, stacked and aligned using AstroImageJ (Collins et al. 2017). The field of view is 2.6 × 2.4 arcmin^2.

broker (Smith et al. 2019).[1] After the discovery, the *BgVri*-bands were followed by the Las Cumbres Observatory Global Telescope network (LCO; Brown et al. 2013) and reduced using the BANZAI pipeline (McCully et al. 2018). Full *BgVri*-band photometry was obtained until 23/03/2020 from which point only *Vri*-band photometry could be obtained. Observation was obtained from a combination of 1 m telescopes from the Siding Spring Observatory (code: COJ), the South African Astronomical Observatory (code: CPT), the McDonald Observatory (code: ELP), and the Cerro Tololo Interamerican Observatory (code: LSC). Both *c* and *o*-band photometry were also obtained by the Asteroid Terrestrial-impact Last Alert System (ATLAS; Smith et al. 2020) and reduced through the standard ATLAS pipeline (Tonry et al. 2018). The *BgVri* + *co*-band absolute light curve from the follow-up campaigns are shown in Fig. 2. The photometry has been corrected for reddening using a Milky Way (MW) extinction of $E(B-V)_{\rm MW} = 0.025 \pm 0.001$ mag, obtained using the Galactic dust map calibration of Schlafly & Finkbeiner (2011) and extinction factor $R_V = 3.1$. The host galaxy extinction was taken to be negligible relative to MW extinction, as there was no noticeable Na I D λλ 5890, 5896 lines at the SN rest frame (e.g. Poznanski, Prochaska & Bloom 2012). Also, it should be noted that, as seen in Fig. 1, SN 2020cpg was located far from the galactic centre where the effect of dust is likely reduced. All uncorrected LCO photometry and ATLAS photometry are given in Tables A1 and A2, respectively.

2.3 Spectroscopy

Spectra from multiple telescopes were obtained over an 80-d period post-explosion and reduced through standard means available within each observatory pipeline. The classification spectrum of SN 2020cpg (Poidevin et al. 2020) was obtained with the LT, on 19/02/2020 using the Spectrograph for the Rapid Acquisition of Transients (SPRAT; Piascik et al. 2014) and was reduced by the LT automatic pipeline[2] (see Barnsley, Smith & Steele 2012, for details on the pipeline). Several later spectra were also obtained using the LT. Additional spectra for SN 2020cpg were obtained by the advanced Public ESO Spectroscopic Survey for Transient Objects (ePESSTO +)[3] (Smartt et al. 2015), using the ESO Faint Object Spectrograph and Camera mounted on the New Technology Telescope (NTT; EFOSC2; Buzzoni et al. 1984). ePESSTO + data were reduced as described in Smartt et al. (2015). The Alhambra Faint Object Spectrograph and Camera (ALFOSC) mounted on the Nordic Optical Telescope (NOT; Djupvik & Andersen 2010) provided several spectra of SN 2020cpg, which were reduced by the Foscgui pipeline.[4] Multiple spectra were taken by the LCO 2 m Faulkes Telescope South (FTS) at COJ and Faulkes Telescope North (FTN) at the Haleakala Observatory (code: OGG). We attempted to obtain further spectra after two and a half months post-explosion; however, SN 2020cpg was too dim at this point for the available telescopes to obtain good-quality spectra. All spectra have been binned to improve the S/N ratio, and de-reddened, assuming a standard $R_V = 3.1$ and the $E(B-V)$ given in Section 2.1. All spectra can be seen in Fig. 3. The details on the phase from *B*-band max, observatory and instrument alongside the observed range are given in Table 1.

3 METHOD

3.1 Pseudo-bolometric light curve

From the *BgVri*-band photometry obtained for SN 2020cpg, we constructed a pseudo-bolometric light curve, shown in Fig. 4, using the pseudo-bolometric light curve code of Nicholl (2018). As we lack any ultraviolet (UV) or near-infrared (NIR) data, we approximate the missing luminosity in these bands by extrapolating the blackbody spectral energy distributions that were fit to the *BgVri*-bands into the UV and NIR regions. The UV and NIR contributions to the pseudo-bolometric light curve are relatively small at peak time, contributing ∼ 10–20 per cent and ∼ 15–25 per cent, respectively, compared to the optical contribution, which accounts for ∼ 50–60 per cent of total flux near bolometric peak (Lyman, Bersier & James 2013). We conclude that our extrapolation to UV and NIR bands does not introduce a significant error to the bolometric light curve.

Along with the pesudo-bolometric light curve of SN 2020cpg, we construct pesudo-bolometric light curves for SN 1993J (Richmond et al. 1994; Barbon et al. 1995; Richmond et al. 1996), SN 2003bg (Hamuy et al. 2009), SN 2008ax (Pastorello et al. 2008; Tsvetkov et al. 2009), SN 2009jf (Sahu et al. 2011; Bianco et al. 2014), SN 2011dh (Tsvetkov et al. 2012; Sahu, Anupama & Chakradhari 2013; Brown et al. 2014), iPTF13bvn (Brown et al. 2014; Folatelli et al. 2016; Fremling et al. 2016), SN 2013ge (Drout et al. 2016), 2015ap (Prentice et al. 2019), and SN 2016gkg (Brown et al. 2014; Arcavi et al. 2017; Bersten et al. 2018). The comparison between these SE-SNe is shown in Fig. 5. These SE-SNe were chosen, as they all have comprehensive coverage over the first ∼100 d post-explosion, they all have well-defined explosion dates and photospheric velocities both of which are required for the Arnett-like model used to obtain physical parameters. For these SE-SNe, we excluded any UV and NIR data available when constructing the pseudo-bolometric light curve ensuring the effects of the UV and NIR

[1] https://lasair.roe.ac.uk/object/ZTF20aanvmdt/

[2] http://telescope.livjm.ac.uk/TelInst/Inst/SPRAT/

[3] www.pessto.org

[4] http://graspa.oapd.inaf.it/foscgui.html

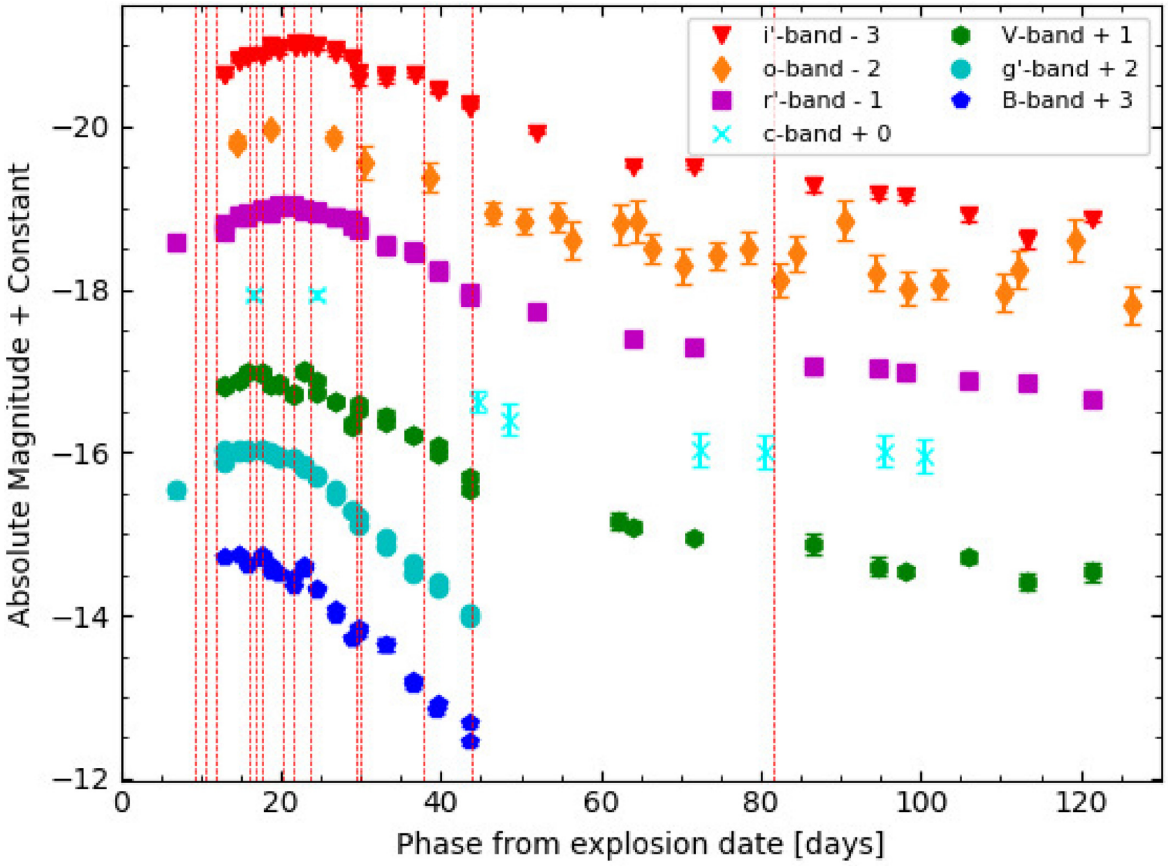

Figure 2. The absolute magnitude photometry of SN 2020cpg in the *BgVri*-bands along with the ATLAS *c* and *o*-band, covering ∼130 d from the explosion date. The individual band light curves have been corrected for extinction, shifted by a constant magnitude and are shown in rest frame. The red dashed lines denote the epochs at which spectra were taken.

extrapolation did not greatly influence the comparison between the SE-SNe. Where SNe lacked Sloan Digital Sky Survey (SDSS) filters, we used the corresponding Johnson–Cousins (J–C) filters to cover a similar wavelength range allowing for a more accurate comparison between the pseudo-bolometric light curves.

3.2 Physical parameters

The bolometric luminosity of an SN is intrinsically linked to several physical parameters, those being the mass of nickel synthesized during the explosion, the amount of material ejected from the outer layers of the progenitor and the kinetic energy of the ejected mass. This relation was first formulated for Type Ia SNe by Arnett (1982) who assumed that all the energy that powers the bolometric light curve originated from the decay of ^{56}Ni → ^{56}Co and the decay of ^{56}Co → ^{56}Fe. While the model was initially formulated for SNe that do not undergo a hydrogen recombination phase, such as those seen in SE-SNe Ib/c and SNe IIb, it has been used regularly for multiple types of SNe. This is done by ignoring the recombination phase and restricting the fitting to the rise and fall of the peak of the bolometric light curve that is powered by radioactive activity, as done in Lyman et al. (2016). The Arnett-like model also assumes that all ^{56}Ni is located in a point at the centre of the ejecta, that the optical depth of the ejecta is constant throughout the evolution of the light curve, the initial radius prior to explosion is very small and that the diffusion approximation used for the model is that of photons. While these assumptions are acceptable, the approximation of constant opacity has a severe effect on diffusion time-scale which is dependent on the estimated ejecta mass and kinetic energy of the SN. The effect of neglecting the time-dependent diffusion on the ^{56}Ni mass was discussed by Khatami & Kasen (2019), who concluded that this results in an over estimation of the ^{56}Ni mass. Through alternative modelling methods it was seen that the ^{56}Ni mass was overestimated by the Arnett-like model by ∼ 30–40 per cent (see e.g. Dessart et al. 2016; Woosley, Sukhbold & Kasen 2020).

We initially used the Arnett-like model to determine the physical parameters of SN 2020cpg and compare the results to several other SE-SNe. In the Arnett-like model the kinetic energy and ejecta mass have a strong dependence on the diffusion time-scale, $\tau_{\rm m}$, of the bolometric light curve, which is given as

$$\tau_{\rm m} = \left(\frac{\kappa_{\rm opt}}{\beta c}\right)^{\frac{1}{2}} \left(\frac{6M_{\rm ejc}^3}{5E_{\rm k}}\right)^{\frac{1}{4}}. \quad (1)$$

Where $M_{\rm ejc}$ is the mass of ejected material and $E_{\rm k}$ is the kinetic energy of the supernovae. Also c is the speed of light, β is the constant of integration derived by Arnett (1982) that takes the value of $\beta \approx 13.8$ and $\kappa_{\rm opt}$ is the optical opacity of the material ejected by the SN. For the Arnett-like model, a constant value of $\kappa_{\rm opt} = 0.06 \pm 0.01 {\rm cm}^2{\rm g}^{-1}$ was used. The degeneracy between the ejecta mass and kinetic energy was broken using the photospheric velocity the event obtained from the velocity of the Fe II 5169 Å line measured at maximum bolometric luminosity. This is the epoch when the outer ejecta has the largest

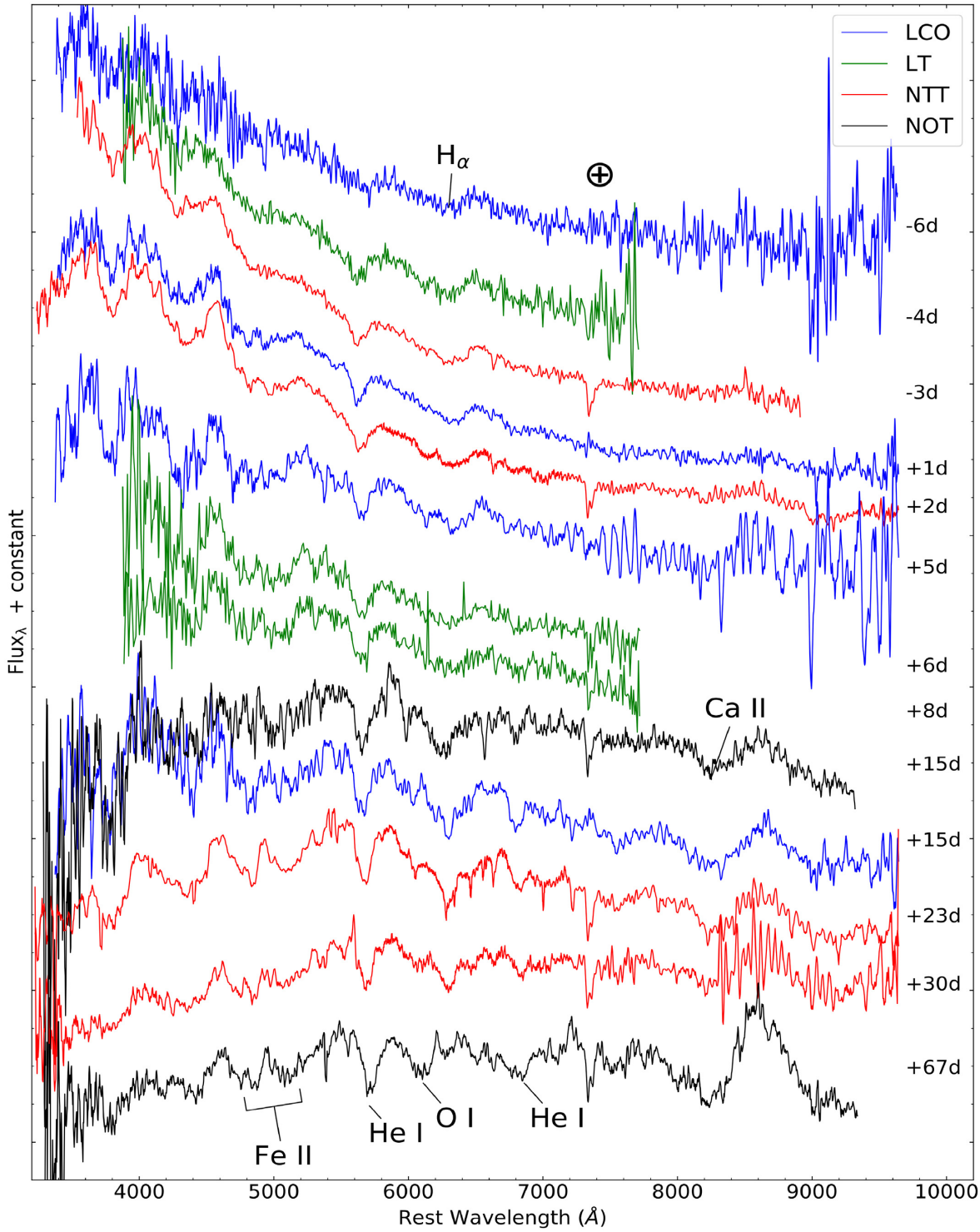

Figure 3. Spectroscopic evolution of SN 2020cpg with details of the observations given in Table 1. The epochs on the right side are relative to B_{max} in rest frame. The H α, He I, Fe II, Ca II, and O I features have been noted along with the main telluric feature at 7600, ⊕. The spectra have been binned to reduce the noise.

contribution to the luminosity under the assumption of homogeneous density. The model was also adjusted to include the SN explosion date to allow for an improved fit and to place a constraint on the rise time of the SNe. For SNe with well observed pre-maximum and well-defined explosion dates we use the dates provided. The explosion date of SN 2020cpg was obtained by constraining the fitting to limit the potential explosion date to after the date of last non-detection and prior to the initial observation.

Due to the known problems with the Arnett-like model, in Section 5.3 we discuss an alternative method for determining the ejecta mass and kinetic energy of SN 2020cpg by comparing the light curve properties and physical properties determined by hydrodynamical

Table 1. Details of the spectroscopic observations of SN 2020cpg. Phase from both the predicted explosion date ($\text{Phase}_{\text{exp}}$) and the date of B_{max} ($\text{Phase}_{B_{\text{max}}}$) are given in rest frame.

Date	$\text{Phase}_{\text{exp}}$ (d)	$\text{Phase}_{B_{\text{max}}}$ (d)	Telescope+ Instrument	Range (Å)
17/02	+ 9	−6	FTS en12	3500–10000
19/02	+ 11	−4	LT SPRAT	4000–8000
20/02	+ 12	−3	NTT EFOSC2	3685–9315
24/02	+ 16	+ 1	FTN FLOYDS	3500–9000
25/02	+ 17	+ 2	NTT EFOSC2	3380–10320
28/02	+ 20	+ 5	FTS en12	3500–10000
29/02	+ 21	+ 6	LT SPRAT	4000–8000
02/03	+ 23	+ 8	LT SPRAT	4000–8000
09/03	+ 30	+ 15	NOT ALFOSC	3200–9600
09/03	+ 30	+ 15	FTN FLOYDS	3500–10000
17/03	+ 38	+ 23	NTT EFOSC2	3380–10320
23/03	+ 44	+ 30	NTT EFOSC2	3380–10320
30/04	+ 82	+ 67	NOT ALFOSC	3200–9600

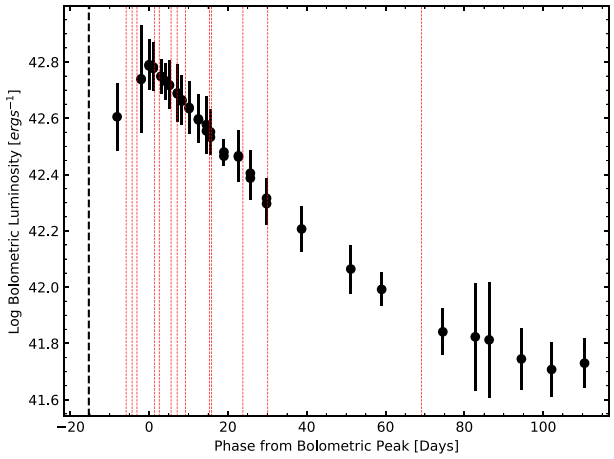

Figure 4. The pseudo-bolometric light curve of SN 2020cpg constructed from the *BgVri* photometry. Luminosity is shown relative to days from the peak of the pseudo-bolometric light curve in rest frame and follows approximately 120 d from explosion. The red dashed lines indicate the epochs where spectra were taken and the black dashed line is the yielded explosion date.

modelling of other SE-SNe, as done for SN 2010ah in Mazzali et al. (2013, here after PM13). This method re-scales the physical parameters of other SE-SNe using equation (1) under the assumption that the optical opacity of the two SNe are equivalent. This is physically a more robust assumption than a fixed opacity for all SE-SNe as adopted by the Arnett-like model. A comparison between the results obtained from the Arnett-like model and the PM13 model is presented later in Section 5.3.

4 RESULTS

4.1 Multicolour light curves

The early time rise of both the *B*- and*V*-bands were missed in the follow-up campaign; however, the peaks in both bands were observed, shown in Fig. 2. The bluer bands peaked several days before the red bands, $t^{\text{rise}}_{\text{blue}} \approx 15$ d post-explosion and $t^{\text{rise}}_{\text{red}} \approx 19$ d, see Table 2. Both the *B* and *g* bands were followed for ∼30 d by LCO before the photometry bands dropped below the brightness threshold

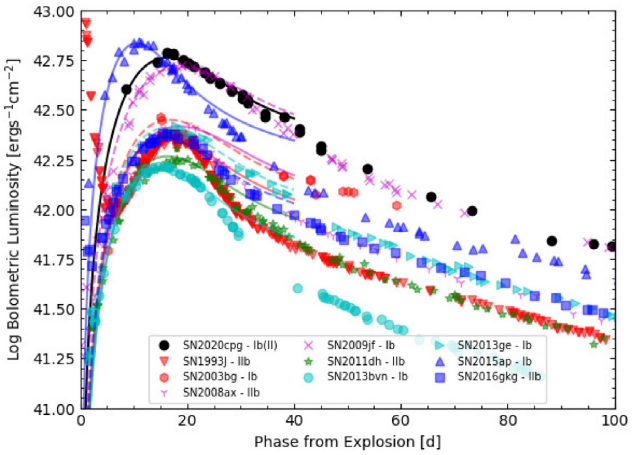

Figure 5. Pseudo-bolometric light curves of SN 1993J, SN 2003bg, SN 2008ax, SN 2009jf, SN 2011dh, iPTF13bvn, SN 2013ge, SN 2015ap, SN 2016gkg, and SN 2020cpg, covering a period of 100 d from their estimated explosion date. The Arnett-like model fit to the pseudo-bolometric light curves, detailed in Section 3.2, are shown as lines and were fitted out to ∼40 d before they started to strongly diverge from the pseudo-bolometric light curves. The velocities used to break the degeneracy for each SN, along with the predicted physical parameters, are given in Table 4.

Table 2. Epoch of light-curve maximum, rise time in rest frame, and peak absolute magnitude for the *BgVri* photometry bands for SN 2020cpg.

Band	MJD_{max}	Rise time (d)	m_{max}	M_{max}
B	58902.1	14.7 ± 2.5	18.38 ± 0.02	−17.75 ± 0.39
g′	58903.1	16.0 ± 2.1	18.05 ± 0.02	−18.04 ± 0.40
V	58904.7	17.0 ± 2.1	18.16 ± 0.02	−17.91 ± 0.38
c	58906.0	18.8 ± 2.3	18.10 ± 0.05	−17.97 ± 0.38
r′	58906.2	18.6 ± 2.1	18.06 ± 0.02	−18.00 ± 0.38
o	58908.3	21.1 ± 2.4	18.05 ± 0.05	−18.01 ± 0.39
i′	58909.2	22.0 ± 2.1	18.05 ± 0.02	−18.00 ± 0.38

required for follow-up. The brightness for the *B* and *g* bands fell by ∼2 mag in the 30 d from the photometric peak, as a result of the SN rapidly cooling. The remaining bands fell at a slower rate, dropping by roughly 1 mag in the same time period, before their decline slowed down as the light curve transitioned to the exponential tail produced by the radioactive decay ^{56}Co synthesized in the explosion. The ATLAS *c*-band was followed for approximately 100 d from the expected explosion date with the *o* band being followed for a further 30 d. The peaks in both bands were not well observed, especially in the *c*-band. As with the other bands the redder *o*-band declines at a slower rate just after maximum light when compared to the *c*-band. The ATLAS bands have a greater error associated with them compared to the *BgVri*-bands, and as the ATLAS bands cover a similar wavelength range as the *BgVri* they were not used when constructing the pseudo-bolometric light curve.

The light curves for He-rich CC-SNe display a variation within the evolution of their light curves due to the range of progenitor properties. As such the *BgVri*-band photometry for SN 2020cpg was compared with those of SN 1993J, SN 2003bg, SN 2009jf, SN 2011dh, iPTF13bvn, SN 2013ge, SN 2015ap, and SN 2016gkg. The absolute magnitude photometry for these SNe relative to SN 2020cpg is shown in Fig. 6, with the details on each SN given in Table 3. SN 2020cpg is brighter than the majority of the other SNe that we compare to, with only SN 2009jf and SN 2015ap being

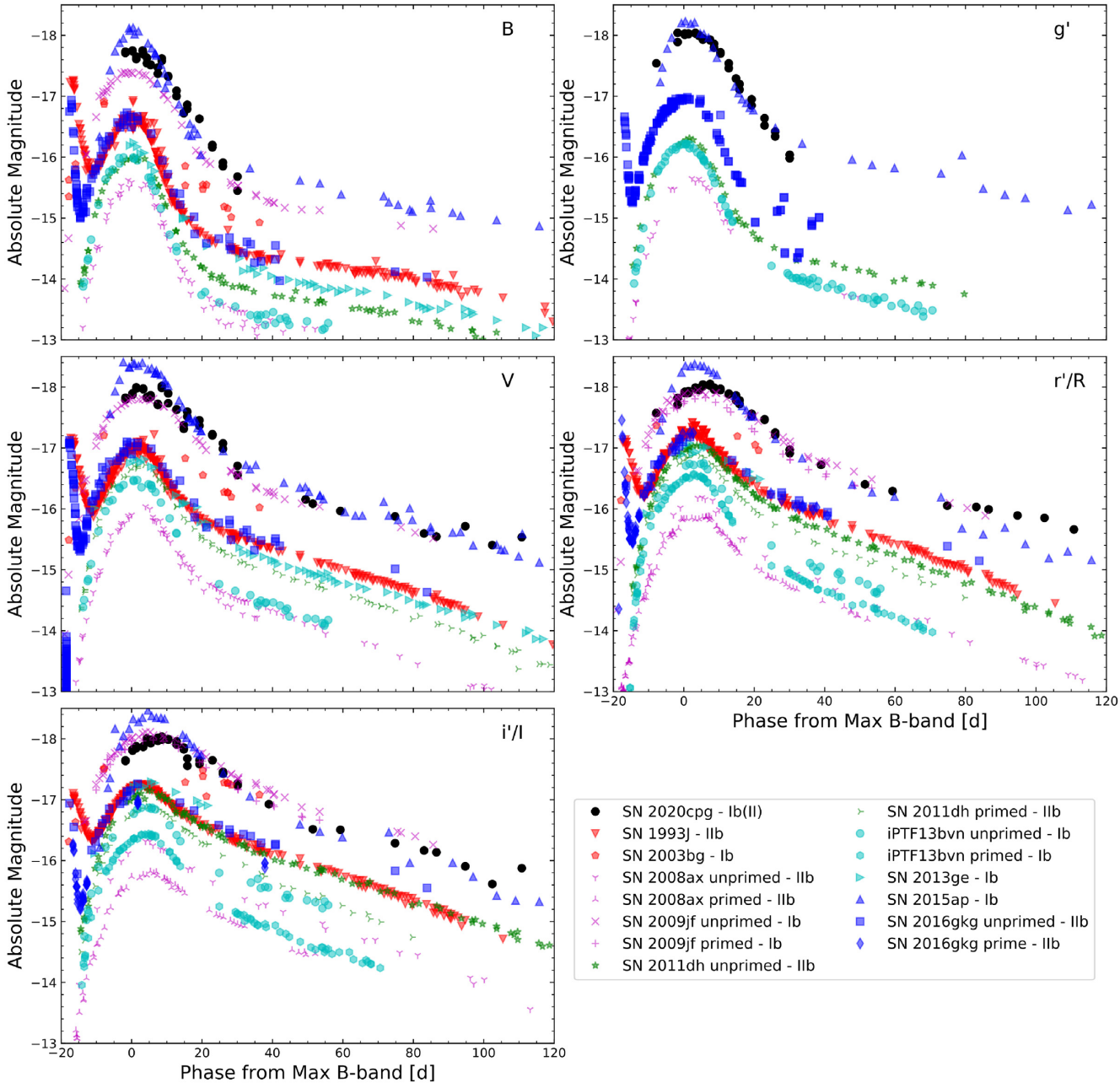

Figure 6. Comparison of the absolute magnitude light curves of several SNe Ib and IIb with SN 2020cpg. All photometry is relative to B_{max} light that was either taken from the literature or by fitting a Gaussian to the *B*-band peak. The light curves have been corrected for time dilation as well as corrected for both Milky Way and host galaxy reddening when possible. Primed bands are SDSS photometry bands and unprimed are the J–C photometry bands. Error on absolute magnitudes not included.

of similar brightness. The *B* and*g* bands evolve in a similar way to that of SN 2015ap, while the other bands evolve more similar to SN 2009jf. Due to the lack of pre-maximum light observations, it is not possible to determine if SN 2020cpg had a shock breakout cooling peak similar to that seen in several other SE-SNe, such as SN 1993J and SN 2016gkg.

4.2 Pseudo-bolometric light curves

The pseudo-bolometric rise time for SN 2020cpg is $t_{\rm rise}^{\rm bol} \approx 16.0 \pm 2.5$ d. Once peak luminosity had been reached the light curve rapidly declines for the next ≈34 d before settling on the exponential tail. Due to lack of much pre-peak photometry, the rise of the pseudo-bolometric light curve is not as well constrained as the post-peak light curve. SN 2020cpg reaches a peak luminosity of $\log(L_{\rm max}) = 42.78 \pm 0.08$ [erg s^{-1}], which is higher than the average luminosity of Type IIb + Ib(II), which has a value of $\log(L_{\rm max}) = 42.2^{+0.4}_{-0.1}$ [erg s^{-1}], and the average maximum luminosity of Type IIb + IIb(I), $\log(L_{\rm max}) = 42.09 \pm 0.17$ [erg s^{-1}], as given in Prentice et al. (2019), showing that SN 2020cpg lies at the brighter end of the SE-SNe regime.

We fit the pseudo-bolometric light curve of SN 2020cpg with the Arnett-like model, using a photospheric velocity of $v_{\rm ph}$ ≈12500 ± 1500 km s^{-1} to break the degeneracy between the kinetic

Table 3. Details for several historical Type Ib and IIb SNe which have been compared to SN 2020cpg.

SN	Explosion date (MJD)	B_{max} date (MJD)	Redshift	Distance (Mpc)	$E(B-V)_{MW}$ (mag)	$E(B-V)_{Host}$ (mag)	Reference
1993J	49072.0	49093.48	−0.000113	2.9	0.069	0.11	1, 2, 3
2003bg	52695.0	52718.35	0.00456	20.25	0.018	-	5
2008ax	54528.8	54546.86	0.001931	5.1	0.0188	0.28	4, 6
2009jf	55101.33	55120.91	0.0079	31	0.097	0.03	7, 10
2011dh	55712.5	55730.82	0.001638	7.25	0.0309	0.05	8, 9, 11
iPTF13bvn	56458.17	56474.95	0.00449	19.94	0.0436	0.17	11, 12, 13
2013ge	56602.5	56618.93	0.004356	19.342	0.0198	0.047	14
2015ap	57270.0	57283.0	0.01138	50.082	0.037	–	17
2016gkg	57651.15	57669.67	0.0049	21.8	0.0166	0.09	11, 15, 16
2020cpg	58887.6	58902.07	0.037	158.6	0.0246	–	–

References. 1: Richmond et al. (1994), 2: Barbon et al. (1995), 3: Richmond et al. (1996), 4: Pastorello et al. (2008), 5: Hamuy et al. (2009), 6: Tsvetkov et al. (2009), 7: Sahu et al. (2011), 8: Tsvetkov et al. (2012), 9: Sahu et al. (2013), 10: Bianco et al. (2014), 11: Brown et al. (2014), 12: Fremling et al. (2016), 13: Folatelli et al. (2016), 14: Drout et al. (2016), 15: Arcavi et al. (2017), 16: Bersten et al. (2018), and 17: Prentice et al. (2019).

Table 4. Physical properties of several SE-SNe derived from the fitting of the Arnett-like model described in Section 3 and shown in Fig. 5. The photospheric velocity used for each SN was taken from their discovery paper.

SN	v_{ph} (km s^{-1})	M_{Ni} ($M_\odot$)	M_{ejc} ($M_\odot$)	E_k (10^{51}erg)
1993J	8000 ± 1000	0.11 ± 0.03	2.0 ± 0.8	0.8 ± 0.3
2003bg	10000 ± 500	0.13 ± 0.04	2.8 ± 0.9	1.7 ± 0.5
2008ax	7500 ± 500	0.14 ± 0.04	2.6 ± 1.0	0.9 ± 0.3
2009jf	11000 ± 500	0.27 ± 0.09	4.0 ± 1.4	2.9 ± 1.0
2011dh	7000 ± 1000	0.09 ± 0.02	1.8 ± 0.5	0.5 ± 0.1
iPTF13bvn	8000 ± 1000	0.07 ± 0.02	1.7 ± 0.4	0.6 ± 0.2
2013ge	10500 ± 500	0.12 ± 0.03	2.7 ± 0.8	1.8 ± 0.5
2015ap	16000 ± 1000	0.22 ± 0.05	1.4 ± 0.4	2.2 ± 0.6
2016gkg	8000 ± 1000	0.10 ± 0.02	1.9 ± 0.4	0.7 ± 0.2
2020cpg	12500 ± 1200	0.27 ± 0.08	3.4 ± 1.0	2.9 ± 0.9

energy and ejecta mass. The value of v_{ph} was obtained from the average Fe II line velocities at peak light. The average value of the Fe II triplet was used instead of the commonly employed Fe II λ 5169 line due to the low signal-to-noise ratio within the Fe II region of the spectrum taken around peak luminosity. From the Arnett-like model fit to SN 2020cpg's pseudo-bolometric light curve, we derive a nickel mass of M_{Ni} =0.27 ± 0.08 $M_\odot$. The ejecta mass and kinetic energy given by the fit had a value of M_{ejc} =3.4 ± 1.0 $M_\odot$ and E_k =2.9 ± 0.9 × 10^{51} erg, respectively. This process was then repeated for the bolometric light curves of the other SE-SNe shown in Fig. 5 and the derived physical parameters are given in Table 4. As expected the Arnett-like model deviates from the pseudo-bolometric light curves at later times ($t \gtrsim 40$ d) when the SNe start to transition into the nebular phase. Relative to the other SNe, SN 2020cpg has a high nickel mass similar to both SN 2009jf and SN 2015ap, shown in Table 4. The similar M_{Ni} between SN 2020cpg and both SN 2009jf and SN 2015ap is expected from their comparable peak luminosities. The ejecta mass and kinetic energy of SN 2020cpg is also higher than the majority of the SE-SNe, we have looked at suggesting that the progenitor of SN 2020cpg was a high-mass star prior to the stripping of the outer envelope. However, due to the problems associated with the Arnett-like approach, we discuss an alternative approach to obtain the values for M_{ejc} and E_k in Section 5.3, we then use the values for M_{ejc} and E_k derived using the PM13 method to estimate the progenitor mass.

4.3 Spectral evolution and comparison

At early times, the spectra of SN 2020cpg (Fig. 3) shows a large blue excess. The spectra rapidly cool until around +15 d from B_{max}. Prominent He I lines are present throughout the spectral evolution with the He I 5876 Å line being the most prominent and the 6678 Å line becoming stronger at around +23 d. Around +1 d post B_{max}, the spectrum develops an absorption feature located in the H α region that persists for ∼30 d. At earlier times during the spectral evolution, the H α feature is split into a high-velocity and low-velocity components that merge into a single H α feature at later times. The presence of the H α line provides strong evidence that SN 2020cpg is not a standard Type Ib SN and may be an intermediate SN between the H-rich and H-poor SE-SNe. While the feature around 6300 Å may be interpreted as the presence of silicon, this is not likely, because it would imply that absorption from other silicon transitions, around 4100 and 5900 Å should be detected in this and later spectra which is not observed. Moreover, when identified as silicon, the line shift would indicate a velocity of 3000 km s^{-1} which is far too slow for this epoch. These pieces of evidence alongside the lack of silicon in the spectra of other well-observed Type Ib/c SNe give strong evidence that the feature is the result of the presence of hydrogen within the outer envelope. Later, the spectral evolution shows the development of Fe II λλ4924, 5018, 5169 lines, although it should be noted that the Fe II lines are located close to He I lines making the separation of these lines difficult, especially given the high noise in this region of the spectra.

The evolution of the line velocities for H α, He I λλ5876, 6678, 7065 and Fe II λλ4924, 5018, 5169 were determined by the fitting of a Gaussian to each feature to locate the minima. The line evolution of each elemental feature is shown in Fig. 7. The line velocities derived from the Gaussian fits are given in Fig. 8. The main source of error for these elemental line velocities comes from the low S/N of the spectra, especially on the fringes where the Fe II line is located, which makes the fitting of the Gaussian more difficult. This results in an error derived from the Gaussian fitting of approximately 15 per cent, with a negligible error associated with the redshift. For the H α feature, we separate the minimum into two distinct high- and low-velocity components. The high-velocity feature is visible from the second spectrum, −4 d, until approximately +15 d post B_{max}, as shown by the solid red line in Fig. 7. At this point, the high-velocity and low-velocity components blend together in the later spectra to form a single H α feature. There is a clear separation between the high- and low-velocity H α components, with the low velocity remaining

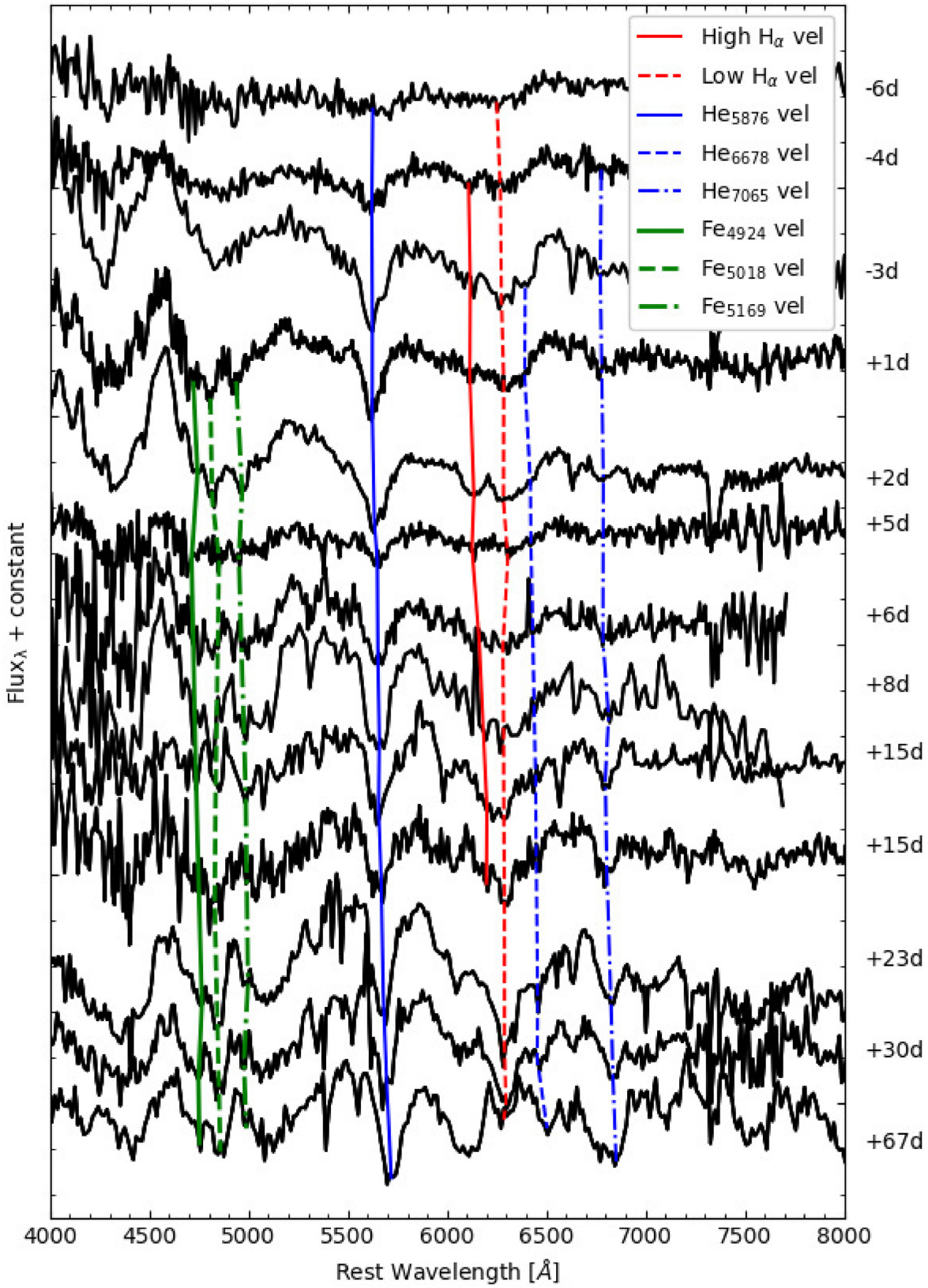

Figure 7. Evolution of SN 2020cpg spectra. The spectra have been plotted between 4000 and 8000 Å to highlight the regions where prominent H α, He I, and Fe II features are visible. The different elements are shown by the different lines, with H α = red, He I = blue, and Fe II = green, and different element lines given by different styles. Lines are only shown when line features are clearly visible within the spectra.

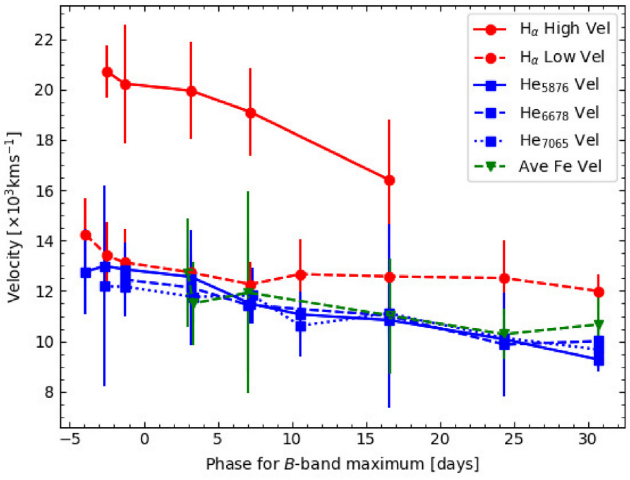

Figure 8. Line velocity evolution of H α, He I, and Fe II from Gaussian fits to the spectra. The H α (red) is split into a high-velocity component and a low-velocity component, shown as the solid line and dashed line, respectively. The evolution of a selection of individual He I spectral lines (blue) are shown as separate curves. Due to the uncertainty in the Fe II lines (green), as a result of the noise in that region of the spectrum, the average line velocity is displayed. The plot is cut-off at ∼30 d due to the emergence of other lines around the H α region.

relatively constant in velocity with a decline of ∼2000 km s^{-1} from ∼14500 to ∼12500 km s^{-1}, while the high velocity component drops by ∼5000 km s^{-1} from ∼21000 to ∼16500 km s^{-1} before the lines seem to merge into one constant H α feature. The He I λ5678 feature remains strong throughout the spectral evolution while the He I λ6678 feature, while not always visible due to high noise, follows the velocity evolution of He I λ5876. The signal-to-noise ratio in the Fe II region made finding the velocity evolution harder than for the other lines. The velocity of the He I and Fe II lines all follow a similar trend declining from ∼13000 km s^{-1}to ∼10000 km s^{-1}. From the velocity evolution, we determine that the photospheric velocity of SN 2020cpg at peak luminosity has an average value of 12500 ± 1200 km s^{-1}, taken from the velocity of the He I and average Fe II features.

We compare the spectra of SN 2020cpg, a H-rich (SN 2011dh), and a H-poor (SN 2015ap) SN, within the range 4000–9000 Å presenting the evolution of the hydrogen features and the line strength relative to standard SNe Ib and IIb, see Fig. 9for the comparisons and Table 5 for the details on the ipectra. Both SN 2011dh and SN 2015ap were close, well observed, SE-SNe allowing for clear comparisons to SN 2020cpg. This is especially true of SN 2015ap, which photometrically appears similar to SN 2020cpg in both shape and luminosity. The epochs chosen were relative to the peak of the pseudo-bolometric light curve so that all SNe were at similar stages in their evolution. The epochs compared are −5, 0, +5, and + 30 d relative to peak luminosity. The grey region in Fig. 9 highlights the H α region. It is clear that early on the spectra of SN 2020cpg are more similar to those of SN 2015ap, especially in the He I lines velocity (∼12000 km s^{-1}), and lack of a strong H α feature. The He I λ6678 feature, which can sometimes blend with the H α feature is not well defined in SN 2020cpg at all epochs and can only be clearly seen in plots b and d of Fig. 9. As the spectra evolve, the He I features of SN 2015ap and SN 2020cpg deepen in a similar fashion, although the H α feature of SN 2020cpg also becomes deeper and more defined. The emergence of the H α feature results in the spectra of SN 2020cpg becoming more 2011dh-like and less like those of SN 2015ap. In the final plot, the spectrum of SN 2020cpg becomes very similar to that of SN 2011dh, especially in the H α region where there is a clear H α absorption feature that is not present in the SN 2015ap spectrum. Throughout the emergence of the H α feature its strength remains weaker than or similar to that of the He I λ5876 peak, compared to the ratio of their strength seen in the SN IIb where the H α feature dominates throughout the spectra. From the classification scheme of Prentice & Mazzali (2017) and the strength of the H α feature relative to the He I peak, it seems that SN 2020cpg should be categorized as a Type Ib(II) SN.

5 DISCUSSION

With a maximum luminosity of 6.03 ± 0.01 × 10^{42} erg s^{-1}, SN 2020cpg is brighter than the average SE-SNe. Among the SNe we have considered here, only SN 2009jf and SN 2015ap have similar luminosities to SN 2020cpg. This suggests that SN 2020cpg is brighter than the average SE-SNe. We also compare the maximum luminosity of SN 2020cpg to the median peak luminosity of SNe Ib + Ib(II) and SNe IIb + IIb(I) in Prentice et al. (2019) showing that SN 2020cpg is located at the brighter end of the luminosity range displayed by H-rich SNe. The rise time of SN 2020cpg is similar to most other SNe we have looked at, although the pseudo-bolometric light curve of SN 2020cpg is broader than many of the SN shown in Fig. 5. The high pseudo-bolometric luminosity indicates a large amount of ^{56}Ni. An Arnett-like model fit yielded a total ^{56}Ni mass of $M_{\rm Ni}$ =0.27 ± 0.08 M$_\odot$. From the analysis of several SE-SNe performed by Prentice et al. (2019), the Arnett-like model derived mean nickel masses of $<M_{\rm Ni}>$=0.07 ± 0.03 M$_\odot$ for SNe IIb + IIb(I) and $<M_{\rm Ni}>$ = 0.09 ± 0.06 M$_\odot$ for SNe Ib + Ib(II). Therefore, SN 2020cpg produced roughly triple the mean nickel mass, placing it on the extreme end of SE-SNe.

Despite the similarity in mean ^{56}Ni between SNe IIb + IIb(I) and SNe Ib + Ib(II), Prentice et al. (2019) showed that SNe Ib + Ib(II) ^{56}Ni masses display a bimodal distribution with a high-mass region, where the ^{56}Ni mass of SN 2020cpg resides. From the distribution of ^{56}Ni mass given by Prentice et al. (2019), SN 2020cpg behaves like H-poor SE-SNe. It should be noted that most neutrino-driven explosion models cannot produce $M_{\rm Ni}$ greater than ∼0.23 M$_\odot$ (Suwa, Tominaga & Maeda 2018), although a study of literature $M_{\rm Ni}$ values done by Anderson (2019) found that ∼ 30 per cent of hydrogen-poor SE-SNe and ∼ 7 per cent of hydrogen-rich SE-SNe have ^{56}Ni masses that are greater 0.23 M$_\odot$. This discrepancy arises from the assumptions of the Arnett-like model (see Section 3.2), which result in an overestimation of the $M_{\rm Ni}$. Taking into account this overestimation the $M_{\rm Ni}$ of SN 2020cpg is reduced to ≈0.16−0.19 M$_\odot$, placing SN 2020cpg's $M_{\rm Ni}$ within, although close to, the upper limits of neutrino-driven explosion models. However, as we have compared the $M_{\rm Ni}$ of SN 2020cpg with other ^{56}Ni masses derived by the Arnett-like model and there is uncertainty in the overestimation of the model, we use the value of mass of ^{56}Ni derived from the Arnett-like model as the upper limit of $M_{\rm Ni}$ for SN 2020cpg.

5.1 Hydrogen envelope

As seen for the spectroscopic evolution of SN 2020cpg when compared to well observed Type Ib and IIb SNe, there is strong evidence for the presence of a hydrogen envelope surrounding the progenitor of SN 2020cpg. The separation of the H α feature into a high-velocity component and a low-velocity component suggests that the hydrogen is located in two distinct regions within the outer envelope of the

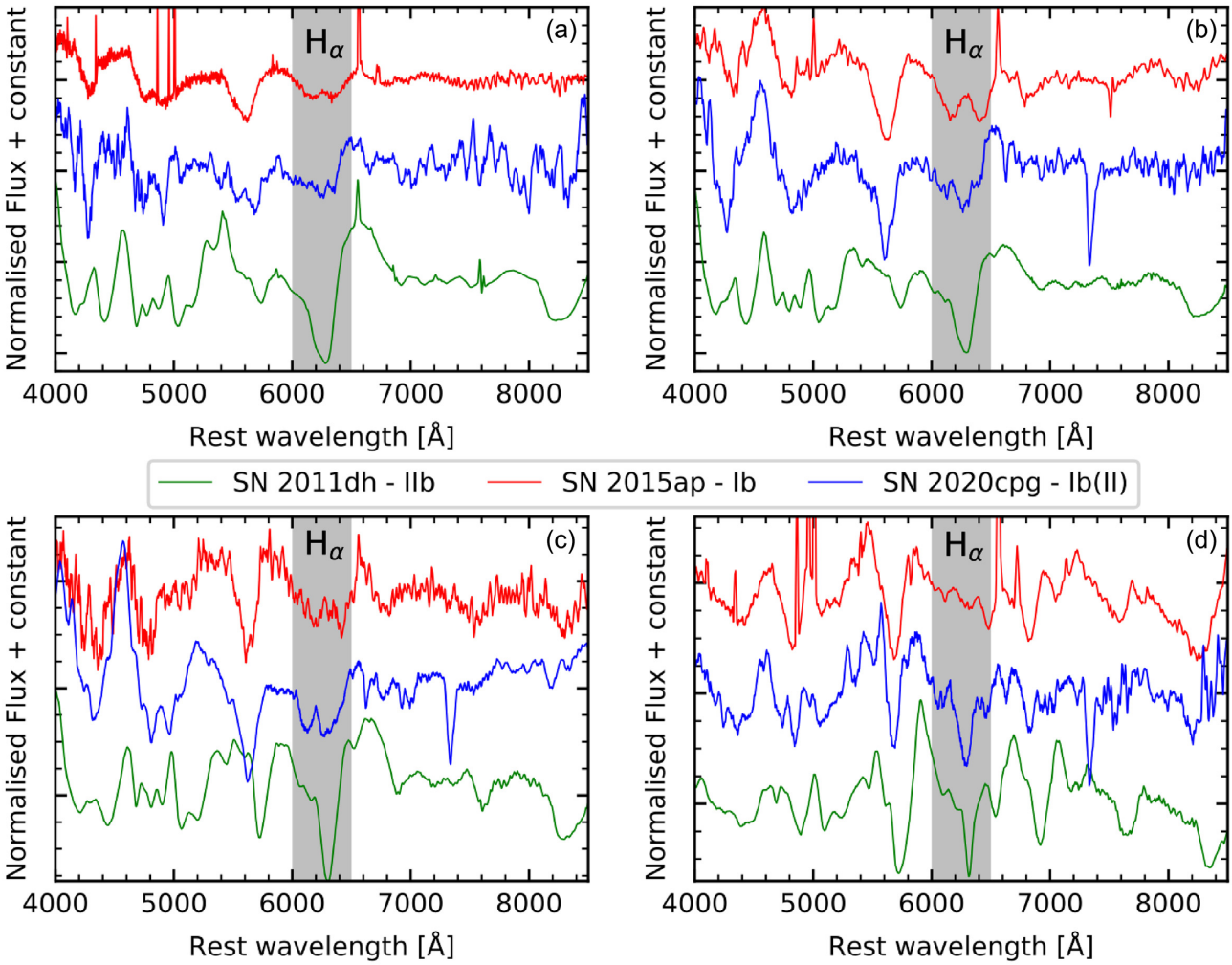

Figure 9. Comparison of SN 2020cpg (blue) with a characteristic SN Ib (SN 2015ap, red) and a characteristic SN IIb (SN 2011dh, green) at several epochs relative to pseudo-bolometric peak. The epochs shown are around (a) −5 d, (b) +0 d, (c) +5 d, and (d) +30 d. The grey-shaded area denotes the region where the H α feature should be located if hydrogen is present within the outer envelope of the progenitor. The spectrum used for each of the plots along with the instrument used to obtain them are detailed in Table 5 and can all be foundwithin the data repository WiseRep (Yaron & Gal-Yam 2012).

Table 5. Spectral details for the spectra used in Fig. 9, including the date the spectra were obtained and the instrument used to obtain them.

SN	Plot	Date	Instrument	Reference
2011dh	a	12/06/2011	FOS_1	1
	b	17/06/2011	ALFOSC	2
	c	25/06/2011	ALFOSC	2
	d	14/07/2011	ALFOSC	2
2015ap	a	15/09/2015	KAST	3
	b	20/09/2015	FLOYDS_S	4
	c	23/09/2015	FLOYDS_N	4
	d	20/10/2015	KAST	3
2020cpg	a	17/02/2020	COJ en12	–
	b	20/02/2020	EFOSC2	–
	c	23/02/2020	EFOSC2	–
	d	23/03/2020	EFOSC2	–

Note. All spectra shown in this table and Fig. 9 are from the following references – 1: Arcavi et al. (2011), 2: Ergon et al. (2014), 3: Shivvers et al. (2019), 4: Prentice et al. (2019).

progenitor star. A thin outer envelope and an inner section where the hydrogen and helium are thoroughly mixed together corresponding to the high-velocity and low-velocity component, respectively. While the two-component H α features are not common among H-rich SE-SNe, it has been observed in other SNe, with SN 1993J displaying a clear double H α feature throughout the photospheric phase. The velocity of the high-velocity component for SN 1993J does not seem as large as that for SN 2020cpg relative to the low-velocity component. This suggests that the amount of hydrogen stripped from the progenitor of SN 2020cpg is greater than that of SN 1993J prior to the explosion, which is further supported by the weak H α feature seen in the spectral evolution of SN 2020cpg. The presence of a weak H α absorption feature provides evidence that SN 2020cpg is not a standard Type Ib SNe but rather a Type Ib(II).

5.2 Model comparisons

By comparing the spectra of SN 2020cpg with model spectra, we can gain insight on the potential elemental composition of the outer layers prior to explosion. Teffs et al. (2020) calculated a set of synthetic SE-SNe models based on a single mass progenitor, with varying degrees of H/He stripping that produces several Type Ic/Ib/IIb analogue SNe. Teffs et al. (2020) estimated the energy of a set of well observed Type

IIb SNe by comparing synthetic and observed spectra at pre-, near-, and post-peak luminosities.

A similar method is applied in this work to SN 2020cpg. The pre- and near-peak spectra of SN 2020cpg are very blue and with few strong features. The early synthetic Type IIb-like spectra in Teffs et al. (2020) are typically redder due to a stronger amount of Fe-group elements mixing, producing strong line blocking in the near UV. As such, the conditions in which the early spectra of SN 2020cpg are produced are beyond the scope of this comparison and can be explored in future work.

We first compare two spectra at approximately +15 and +30 d after *B*-band maximum to the Type IIb model from Teffs et al. (2020) in Fig. 10(a), where the red spectra include the non-thermal effects on hydrogen and the black do not. These non-thermal effects arise from the interactions with energetic electrons that are created by the scattering of gamma rays released from the decay chain of ^{56}Ni and ^{56}Co (Lucy 1991). This Type IIb model has an ejecta mass of $\sim$5.7 $M_\odot$, with 1.3 $M_\odot$ of helium and 0.1 $M_\odot$ of hydrogen. For the earlier spectrum at the top of Fig. 10(a) and when focusing on the H α and He I features, we find the best fit to be that of a 5 foe model that does not include the non-thermal effects on H, where 1 foe is 1×10^{51} erg. The inclusion of non-thermal hydrogen produces a deep and broader H α line that is not reflected in the spectrum of SN 2020cpg. In the second spectrum considered, we instead find that the three foe explosion model matches the spectrum of SN 2020cpg at this late phase. At this lower energy and later phase, the H α line is more narrow and when the non-thermal effects of hydrogen are not included, the 6000–6500 Å region is well reproduced.

As SN 2020cpg has been designated both as a Type Ib and a Type IIb, we also compare our helium rich, but hydrogen free, Type Ib models at the same epochs in Fig. 10(b). For this, we also include the 'best-fitting' models from Fig. 10(a) that do not consider the non-thermal effects of hydrogen as black lines. For the earlier spectrum, we find that the 3 foe Ib model does a reasonable job of reproducing the 6000–6500 Å region without requiring H, but the λ6678 He I is stronger than in the observed spectrum. For the later spectrum, the energy is reduced from the IIb model again to 1 foe and also reproduces this 6000–6500 Å region.

From this, we can infer several properties of the SN 2020cpg regarding its elemental composition. The assumption that helium has non-thermal effects, while H does not is unlikely to be physically viable. However, the mass of hydrogen in the IIb model clearly produces too strong of an H α line. Not including any hydrogen in the model while maintaining a He-rich outer atmosphere results in strong λ6678 and λ7065 He I lines. The re-emission from the H α feature reduces the strength of the λ6678 He I line while affecting the λ7065 He I line less. The best-fitting Ib models having low energy also suggest the He-rich material is confined to lower velocities, such as those below a hydrogen-rich shell as seen in the IIb models. We suggests that a lower mass of hydrogen ($M_{\rm H} < 0.1$ $M_\odot$) could result in a weaker H α feature but still produce enough re-emission to reproduce the 6000–6500 Å region in these late phases. A more detailed model would need to be calculated to derive a stronger estimate on the mass and distribution of H in SN 2020cpg.

At these two epochs, the photosphere has receded deep into the CO-rich region of the ejecta as shown by the presence of the Ca II NIR triplet and the O I λ 7771. Early spectra of Type IIb do not show these features as the abundances of these elements are lower in the H/He-rich shells. Both models are shown with (red line) and without (black line) the non-thermal effects of hydrogen, but both include these effects on the helium. For the Type IIb-like models at these epochs, the spectra that do not treat the non-thermal effects of hydrogen, are better able to reproduce the observed spectral structure between 6000 and 6500 Å that would typically contain a strong H α feature. Due to the depth of the photosphere and the lack of a strong early H α feature, this suggests that the total H α mass is less that 0.1 $M_\odot$ and that the distribution of the hydrogen is further out in the ejecta with respect to the photospheric velocity of the two epochs chosen.

The model shown at the top in Fig. 10(a) is a five foe explosion, with the majority of the 0.1 $M_\odot$ of hydrogen at velocities greater than $\approx$15000 km s^{-1}, while the three foe explosion in the lower model contains hydrogen at velocities greater than $\approx$12000 km s^{-1}. Both models favour both the estimated explosion energy from the Arnett fits in Section 4.2 and the suggestion that some hydrogen is at high velocities. The He I λ 6678 line is relatively too strong for either epoch to match when we do not include non-thermal excitation of the hydrogen. This suggests that a lower mass of hydrogen can still be responsible for some fraction of the 6000–6500 Å feature, likely coincident with Si II causing a re-emission of flux further redwards, reducing the strength of the He I λ 6678 without affecting the He I $\lambda\lambda$5876, 7065, and 7281 lines. However, for a full picture of how the hydrogen and helium are distributed and how much is present, a detailed stratified model would need to be produced, which is beyond the scope of this work.

5.3 Re-scaled light curves

As mentioned in Section 3.2, the Arnett-like model is limited in its viability to obtain realistic ejecta mass and kinetic energy due to the assumption that the optical opacity is constant throughout the bolometric light curve and that the ejecta are optically thick. The problem with these assumptions is that helium is optically transparent at the temperatures reached surrounding the peak light phase of the light curve. In order to account for the effects of the helium layer on the ejecta mass and kinetic energy a detailed hydrodynamical model is required. However, this would not have been easily done with SN 2020cpg due to the lack of early time photometry and the low signal-to-noise ratio for the spectra. In order to estimate the physical parameters for SN 2020cpg, we transform equation (1) to obtain a ratio for the ejecta mass and kinetic energy between SN 2020cpg and other SE-SNe that have detailed hydrodynamical models:

$$\frac{E_{\rm k1}}{E_{\rm k2}} = \frac{\tau_{\rm m1}^2 * v_{\rm ph1}^3 * \kappa_1^{-1}}{\tau_{\rm m2}^2 * v_{\rm ph2}^3 * \kappa_2^{-1}}, \tag{2}$$

and

$$\frac{M_{\rm ejc1}}{M_{\rm ejc2}} = \frac{\tau_{\rm m1}^2 * v_{\rm ph1} * \kappa_1^{-2}}{\tau_{\rm m2}^2 * v_{\rm ph2} * \kappa_2^{-2}}. \tag{3}$$

Here, $\tau_{\rm m}$ is the diffusion time of the light curve, $v_{\rm ph}$ is the photospheric velocity at maximum light, and κ is the optical opacity of the SN ejecta. Due to the difficulty in determining κ, we have assumed that it is the same for both SNe. This assumption holds strong for SNe of the same classification type due to the similar elemental structure between the two SNe and becomes weaker as different types of SN are compared to one another. However, as we will be using only SE–SNe to obtain the ejecta mass and kinetic energy of SN 2020cpg the problem that arises from the use of SNe with different opacities should be minimized.

We compare SN 2020cpg with SN 1993J (Nomoto et al. 1993), SN 1994I (Sauer et al. 2006), SN 2002ap (Mazzali et al. 2002), SN 2003bg (Mazzali et al. 2009), SN 2004aw (Mazzali et al. 2017),

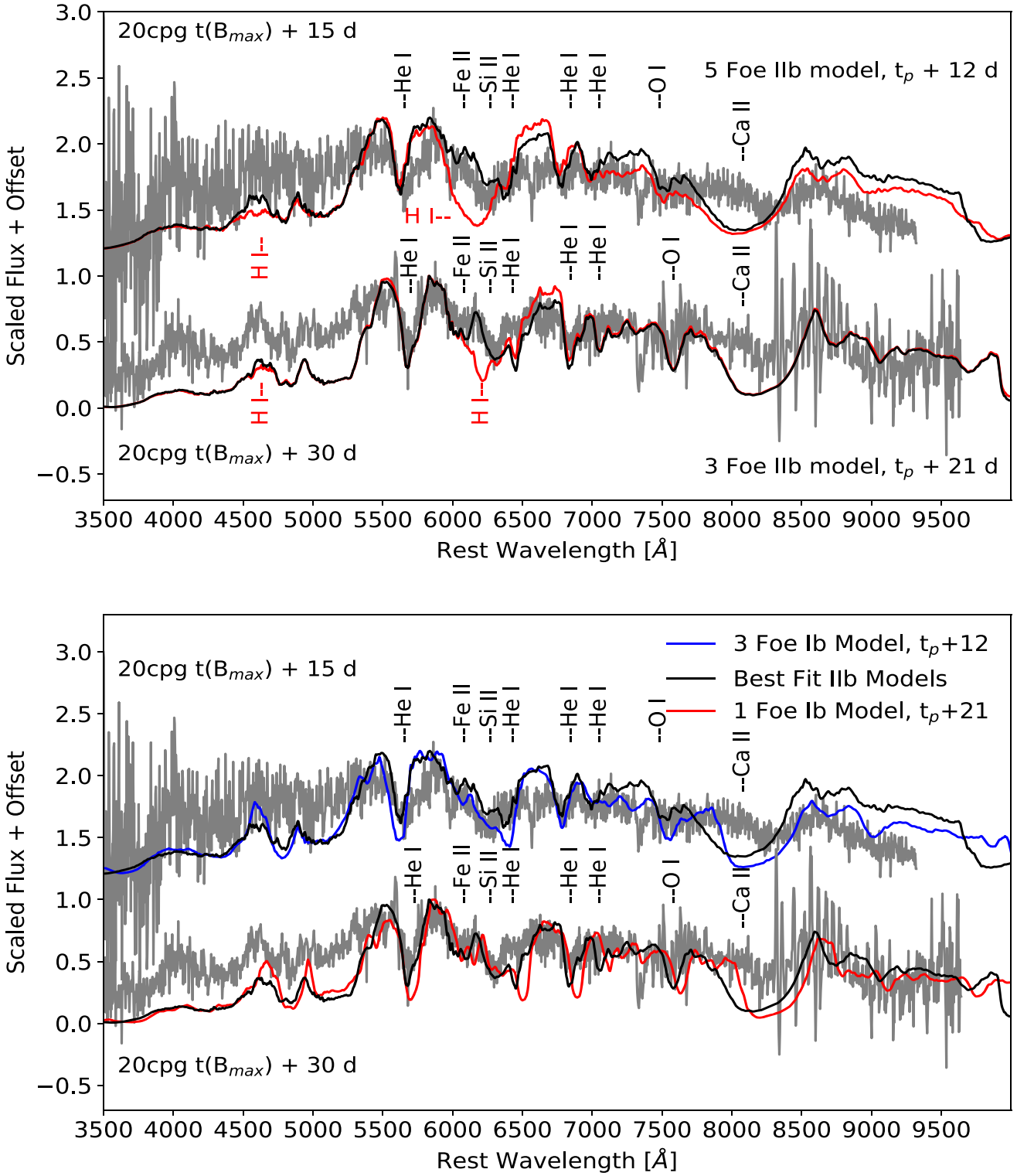

Figure 10. Top: Comparison of SN 2020cpg spectra with two different energy (3 and 5 foe) Type IIb models. Where $t_{\rm p}$ indicates the epoch of bolometric peak. The red model spectra include the non-thermal effects of hydrogen, while the black model spectra omit the non-thermal effects. Both models include the non-thermal effects on He. Several important contributing elements, in particular those near the H α line, are shown above their feature within the spectra. Bottom: SN 2020cpg spectra at +15 and +30 d from *B*-band maximum fit with a IIb-like model and with a Ib model with three foe of energy at a time of +12 d from $t_{\rm p}$ and one foe of energy at a time of +21 d, respectively. The IIb model has an ejecta mass of ≈5.7 $M_{\odot}$, with 1.3 $M_{\odot}$ of helium and 0.1 $M_{\odot}$ of hydrogen.

and SN 2008D (Mazzali et al. 2008; Tanaka et al. 2009), all SE-SNe that have undergone hydrodynamical modelling. Since several of the above SNe, including SN 2020cpg, lack early time photometric data, it was not always possible to determine τ_m. Instead, we used the width of the pseudo-bolometric light curve taken from 0.5 mag below peak light as an alternative to τ_m. Due to the width of the light curve being influenced by both the ejecta mass and kinetic energy, as shown in equation (1), this allowed for a direct comparison between the widths of the light curves and physical properties of SN 2020cpg and the modelled SE-SNe. The details on photospheric velocity and light curve widths for each SN along with the M_{ejc} and E_k of SN 2020cpg given by equations (2) and (3) are shown in Table 6.

We obtain physical parameters for SN 2020cpg, using both the photospheric velocity at pseudo-bolometric peak, $v_{ph}(t = \max)$, for the individual SNe and the photospheric velocity at $t = 16$ d from the reported explosion date, $v_{ph}(t = 16)$. We use $v_{ph}(t = \max)$ to break the degeneracy between the ejecta mass and the kinetic energy, as it would be the velocity of the photosphere when all of the light has diffused through the ejecta. $v_{ph}(t = 16)$ was also used to compare the different SNe at the point when SN 2020cpg had reached maximum pseudo-bolometric light, allowing a direct comparison between SNe to be made. The values for the physical parameters obtained from comparisons with the hydrodynamical models are higher than those derived from using the Arnett-like model, as expected when comparing the Arnett-like model with hydrodynamical models. The main outlier in Table 6 is the properties predicted from the SN 2003bg, a hypernova, which despite having a relatively high kinetic energy possessed a low photospheric velocity at pseudo-bolometric peak, resulting in a low ejecta mass and large kinetic energy.

There is a clear trend in the ejecta mass and kinetic energy obtained using the PM13 method, which arises from the type of SN that SN 2020cpg is compared to, with the He-rich SE-SNe resulting in a generally larger values while the values obtained from He-poor SNe are noticeably lower. As SN 2020cpg is a He-rich SN, we use the physical parameters obtained from the Type Ib and IIb SNe to determine the values of the ejected mass, M_{ejc} $\sim 5.5 \pm 2.0$ $M_\odot$, and kinetic energy, E_k $\sim 9.0 \pm 3.0 \times 10^{51}$ erg, for SN 2020cpg. The value obtained using $v_{ph}(t = 16)$ for the ejecta mass was $\sim 4.0 \pm 1.5$ $M_\odot$ and a kinetic energy of $\sim 5.0 \pm 2.0 \times 10^{51}$ erg. It should be noted that the PM13 model is limited in scope and should not be expected to predict values of both M_{ejc} and E_k to a precision greater than 0.5 $M_\odot$ and 1.0×10^{51} erg, respectively. The values produced using $v_{ph}(t = \max)$ converge on the physical parameters with an average standard deviation of 1.85, while the $v_{ph}(t = 16)$ has an average standard deviation of 1.89. This suggests that using the photospheric velocity at pseudo-bolometric peak for each SN converge on a value better than the photospheric velocity at SN 2020cpg pseudo-bolometric peak. The values for the ejecta mass and kinetic energy produced by the PM13 method are much higher than those predicted by the Arnett-like model, as expected due to the contribution of the helium envelope and the effect of having similar optical opacities. However, the ejecta mass derived from the PM13 method matches the value obtained by comparing the spectra of SN 2020cpg with the spectral models of Teffs et al. (2020), although the kinetic energy given by the modelling is lower than that predicted using the method from PM13.

The ejecta mass given by the spectral modelling and comparison with modelled SE-SNe has a value roughly double that given for Ib + Ib(II) and IIb + IIb(I) by Prentice et al. (2019) that take a mean value of 2.2 ± 0.9 $M_\odot$ and 2.7 ± 1.0 $M_\odot$, respectively. This places SN 2020cpg in the higher mass range of SE-SNe with only one H-rich and two H-poor SE-SNe having similar ejecta mass. The ejecta mass predicted by the Arnett-like model is closer to the mean values given by Prentice & Mazzali (2017), although still greater than the median, showing that by all standards SN 2020cpg was a more massive event than the typical SE-SNe. The lower ejecta mass estimated by the Arnett-like model is expected, as this has been seen in several SNe such as SN 2008D which was estimated to have an ejecta mass of $2.9^{+1.0}_{-0.6}$ $M_\odot$ from an Arnett-like approach (Lyman et al. 2016) and $\sim$5–7 $M_\odot$ from hydrodynamic modelling (Mazzali et al. 2008; Tanaka et al. 2009). When compared to the ejecta masses of the H-rich SE-SNe, SN 2020cpg lies in the region that has been associated with an extended progenitor. As the ejecta mass obtained using the comparative method of PM13 and the spectral modelling of Teffs et al. (2020) are in close agreement, we take the PM13 method as a valid replacement for the Arnett-like model to obtain the ejecta mass when dealing with SE-SNe. The PM13 method will also improve in the future as more SE-SNe undergo hydrodynamical modelling.

From the PM13 method the derived kinetic energy takes a value of $\sim 9.0 \pm 3.0 \times 10^{51}$ erg which is greater than both the spectral modelling and the Arnett-like model. This kinetic energy place SN 2020cpg on the border of the Hypernovae, which are thought to have kinetic energies on the order of 10^{52} erg. The kinetic energy derived from spectral modelling tends towards a lower kinetic energy than the PM13 method, however, larger than the kinetic energy estimated by the Arnett-like model. The Arnett-like model derived a kinetic energy of $\sim 2.9 \pm 0.9 \times 10^{51}$ erg, which is similar to the kinetic energy suggested by the spectral modelling. However, given the high ^{56}Ni mass the kinetic energy derived from the Arnett-like model is unlikely to be enough to synthesize the required amount of nickel.

From the derived ejecta mass, under the assumption that the progenitor did not collapse into a black hole but holds a 1.4 $M_\odot$ neutron star, the progenitors core mass can be assumed to be $M_{ejc} + M_{NS} - M_{outerenvelope} = M_{COcore} \approx 6.0 \pm 2.0$ $M_\odot$. Here, we assumed that the mass of the outer envelope was ~ 1.5 $M_\odot$. This core mass is just higher than the majority of SE-SNe investigated in Prentice & Mazzali (2017), which takes a mean value <5 $M_\odot$. A core mass of $\sim 6.0 \pm 2.0$ $M_\odot$ is thought to originate from a progenitor with an initial mass of 18−25 $M_\odot$ (Sukhbold et al. 2016) suggests that the progenitor of SN 2020cpg would have had a high mass prior to explosion, within the range of 18−25 $M_\odot$.

As mentioned earlier with the Arnett-like model, the opacity for both SN 2020cpg and the comparison SN is neither constant nor the same. To this end, we used equation (1) to obtain an opacity for SN 2020cpg, which had a value of $\kappa_{opt} = 0.10 \pm 0.04$ cm^2 g^{-1}. Using the opacity for SN 2020cpg, we then obtained the opacities of all the SE-SNe we compared with SN 2020cpg, which are shown in Table 7. As expected the He-rich SNe tend to have a lower opacity than the He-poor SNe due to the fact that the helium present within the ejecta is virtually transparent to the optical photons. The opacity for SN 2008D has two values due to the different ejecta masses that we used. By looking at the opacities determined using the above method, it is clear that a single time-independent value of the opacity should not be used for all types of SE-SNe, as done with the Arnett-like model discussed in Section 3.2.

6 SUMMARY AND CONCLUSIONS

The study of SN 2020cpg and the discovery of the weak hydrogen features within the otherwise SN Ib-like spectra shows that formation channels between SNe Ib and IIb are not as rigid as previously

Table 6. SN parameters obtained from detailed hydrodynamic models and the resulting M_{ejc} and E_k for SN 2020cpg using the photospheric velocity obtained at the peak of the pseudo-bolometric light curve and the velocity at $t \sim 16$ d post-explosion, the time that SN 2020cpg peaked. The SNe are ordered by their types with the SNe with the least stripped progenitors at the top and most stripped at the bottom.

								2020cpg			2020cpg	
SN	Type	M_{ejc} ($M_\odot$)	E_k (10^{51} erg)	Reference	$t(L_{max})^a$ (d)	LC width^b (d)	v_{ph}(max)^c (km s^{-1})	M_{ejc} ($M_\odot$)	E_k ($\times 10^{51}$ erg)	v_{ph}(t $\sim$ 16)^d (km s^{-1})	M_{ejc} [$M_\odot$]	E_k [$\times 10^{51}$ erg]
03bg	IIb-Hyper	4.8 ± 0.5	5.0 ± 1.5	6	25.0 ± 2.0	34.0 ± 2.0	7000 ± 500	3.0 ± 1.0	11.0 ± 4.0	9000 ± 500	2.0 ± 1.0	4.0 ± 1.0
93J	IIb	3.7 ± 0.5	1.2 ± 0.1	1	19.0 ± 2.0	18.0 ± 2.0	7500 ± 100	7.0 ± 2.5	6.0 ± 1.0	9500 ± 100	5.0 ± 2.0	3.0 ± 1.0
08D	Ib	7.0 ± 0.5	6.0 ± 0.5	4	19.0 ± 2.0	24.0 ± 2.0	9500 ± 500	6.0 ± 2.0	9.0 ± 2.0	10000 ± 500	5.5 ± 2.0	7.0 ± 1.0
08D	Ib	5.3 ± 1.0	6.0 ± 0.5	5	19.0 ± 2.0	24.0 ± 2.0	9500 ± 500	4.0 ± 2.0	9.0 ± 4.0	10000 ± 500	4.0 ± 2.0	7.0 ± 3.0
04aw	Ic	4.0 ± 1.0	4.5 ± 1.5	7	16.0 ± 1.0	21.0 ± 2.0	11500 ± 500	4.0 ± 2.0	5.0 ± 2.0	11500 ± 500	4.0 ± 2.0	5.0 ± 2.0
94I	Ic	1.2 ± 0.1	1.0 ± 0.5	3	12.0 ± 2.0	11.0 ± 2.0	10000 ± 500	4.5 ± 1.5	6.0 ± 3.0	9000 ± 1000	5.0 ± 2.0	8.0 ± 5.0
02ap	Ic-BL	2.4 ± 1.2	4.0 ± 0.5	2	13.0 ± 2.0	18.0 ± 2.0	12500 ± 1250	3.0 ± 2.0	5.0 ± 1.0	9000 ± 100	4.0 ± 3.0	12.0 ± 3.0

References. 1: Nomoto et al. (1993), 2: Mazzali et al. (2002), 3: Sauer et al. (2006), 4: Mazzali et al. (2008), 5: Tanaka et al. (2009), 6: Mazzali et al. (2009), 7: Mazzali et al. (2017).
[a]Rise time from the explosion to the pseudo-bolometric light-curve peak. [b]Width of pseudo-bolometric light curve taken from 0.5 mag below peak light. [c]Photospheric velocity at epoch of peak light. [d]Photospheric velocity at +16 d from explosion date (same epoch as when SN 2020cpg reached peak light).

Table 7. Opacities derived from the SN 2020cpg opacity. There seems to be a trend with the He-rich SNe having a lower opacity than the He-poor SNe.

SN	Type	Opacity [cm^2 g^{-1}]
03bg	IIb-Hyper	0.27 ± 0.19
93J	IIb	0.06 ± 0.04
08D	Ib	0.08 ± 0.06
08D	Ib	0.13 ± 0.09
04aw	Ic	0.13 ± 0.10
94I	Ic	0.10 ± 0.08
02ap	Ic-BL	0.19 ± 0.16

thought. From the coverage of SN 2020cpg, we were able to compare the evolution of SN 2020cpg with several other SE-SNe. Photometrically, SN 2020cpg looks very similar to the Type Ib SN 2009jf in peak luminosity, although the light curve of SN 2020cpg is slightly broader compared to SN 2009jf. Spectroscopically SN 2020cpg initially looked similar to the Type Ib SN, such as SN 2015ap, with the main difference being the presence of the weak H α feature within the spectra of SN 2020cpg. As the spectra evolve, the H α feature becomes more dominant until it rivals the He I λ5876 feature in strength, making SN 2020cpg resemble more that of a Type IIb SN, such as SN 2011dh. Due to the weak H α feature that is shown within the spectra of SN 2020cpg, we believe that it was a Type Ib(II) SN. As the H α feature grows in strength from the initial spectrum, we suggest that the hydrogen may have existed in a thin envelope as well as mixed into the outer layers of the helium shell prior to the explosion, which became more dominant as the photosphere receded through the mixed hydrogen/helium layer.

SN 2020cpg exploded producing an estimated Nickel mass of $\sim 0.3 \pm 0.1$ $M_\odot$ and from comparisons with hydrodynamic models of well-studied He-rich SE-SNe an ejecta mass of $\sim 5.5 \pm 2.0$ $M_\odot$ and a kinetic energy of $\sim 9.0 \pm 3.0 \times 10^{51}$ erg. From spectral modelling, the amount of helium expected within the ejecta is 1.3 $M_\odot$ with a further 0.1 $M_\odot$ of hydrogen contained within the outer envelope with a large majority of it existing above a velocity of $\approx$15 000 km s^{-1}. From this modelling and the assumption that a neutron star remnant was formed, SN 2020cpg would have had a core mass of $M_{core} = 6.0 \pm 2.0$ $M_\odot$ that corresponds to a progenitor star with an initial mass of $M_{ZAMS} \sim 18-25$ $M_\odot$. Due to the distance to the host galaxy and the position of SN 2020cpg within the host galaxy, it is unlikely that there are any pre-explosion images of high enough quality to allow for the progenitor of SN 2020cpg to be determined. Further modelling of SN 2020cpg may give evidence for the progenitor however that is beyond the scope of this paper.

The use of the PM13 model provides an alternative approach to the Arnett-like model in determining the ejecta mass and kinetic energy of new SE-SNe. The PM13 method accounts for the effects of the helium layer and the time dependency of the optical opacity, both of which are ignored in the Arnett-like approach. The PM13 model produces ejecta masses and kinetic energies that resemble those derived from comparison of optical spectra with spectral models, whereas the Arnett-like approach seems to underestimate these values. Unlike the Arnett-like model, when used on SE-SNe the PM13 model requires several SNe of the same classification to constrain the ejecta mass and kinetic energy. This can lead to some outliers, like hypernovae, distorting the results. However, as more SE-SNe undergo hydrodynamical modelling the constraining power of the PM13 model increases and the effect the outliers have is reduced.

ACKNOWLEDGEMENTS

S.J. Prentice is supported by H2020 ERC grant no. 758638. J.J. Teffs is funded by the consolidated STFC grant no. R27610. This paper is based in part on observations collected at the European Southern Observatory (ESO) under ESO programme 1103.D-0328(J). T.W. Chen acknowledges the European Union Funding under Marie Skłodowska-Curie grant no. H2020-MSCA-IF-2018-842471. L. Galbany was funded by the European Union's Horizon 2020 research and innovation programme under the Marie Skłodowska-Curie grant no. 839090. This work has been partially supported by the Spanish grant no. PGC2018-095317-B-C21 within the European Funds for Regional Development (FEDER). M. Gromadzki is supported by the Polish National Science Center (NCN) MAESTRO grant no. 2014/14/A/ST9/00121. T. Müller-Bravo was funded by the CONICYT PFCHA / DOCTORADOBECAS CHILE/2017-72180113. M. Nicholl is supported by a Royal Astronomical Society Research Fellowship. This work makes use of observations obtained by the Las Cumbres Observatory global telescope network. The LCO team is supported by NSF grant nos AST-1911225 and AST-1911151. Based in part on observations made with the Liverpool Telescope operated on the island of La Palma by Liverpool John Moores University in the Spanish Observatorio del Roque de los Muchachos of the Institutode Astrofisica de Canarias with financial support from the UK Science and Technology Facilities Council. The data presented here were obtained in part with ALFOSC, which is provided by the Instituto de As-trofisica de Andalucia (IAA) under a joint agreement

with the University of Copenhagen and NOTSA, with observation having been made with the Nordic Optical Telescope, operated at the Observatorio del Roque de los Muchachos, La Palma, Spain, of the Instituto de Astrofisica de Canarias. This work has made use of data from the Asteroid Terrestrial-impact Last Alert System (ATLAS) project. ATLAS is primarily funded to search for near earth asteroids through NASA grant nos NN12AR55G, 80NSSC18K0284, and 80NSSC18K1575; by-products of the NEO search include images and catalogues from the survey area. The ATLAS science products have been made possible through the contributions of the University of Hawaii Institute for Astronomy, the Queen's University Belfast, and the Space Telescope Science Institute. Based on observations collected at the European Organisation for Astronomical Research in the Southern Hemisphere, Chile, as part of ePESSTO+ (the advanced Public ESO Spectroscopic Survey for Transient Objects Survey). ePESSTO + observations were obtained under ESO programme ID 1103.D-0328 (PI: Inserra). LCO data have been obtained via OPTICON proposals (IDs: SUPA2020B-002 SUPA2020A-001 OPTICON 20A/015 and OPTICON 20B/003). The OPTICON project has received funding from the European Union's Horizon 2020 research and innovation programme under grant no. 730890.

DATA AVAILABILITY

Data will be made available on the Weizmann Interactive Supernova Data Repository (WISeREP) at https://wiserep.weizmann.ac.il/.

REFERENCES

Anderson J. P., 2019, A&A, 628, A7
Arcavi I. et al., 2011, ApJ, 742, L18
Arcavi I. et al., 2017, ApJ, 837, L2
Arnett W. D., 1982, ApJ, 253, 785
Barbon R., Benetti S., Cappellaro E., Patat F., Turatto M., Iijima T., 1995, A&AS, 110, 513
Barnsley R. M., Smith R. J., Steele I. A., 2012, Astron. Nachr., 333, 101
Bellm E. C. et al., 2019, PASP, 131, 018002
Bersten M. C. et al., 2012, ApJ, 757, 31
Bersten M. C. et al., 2018, Nature, 554, 497
Bianco F. B. et al., 2014, ApJS, 213, 19
Blondin S., Tonry J. L., 2007, ApJ, 666, 1024
Brown T. M. et al., 2013, PASP, 125, 1031
Brown P. J., Breeveld A. A., Holland S., Kuin P., Pritchard T., 2014, Ap&SS, 354, 89
Buzzoni B. et al., 1984, Messenger, 38, 9
Collins K. A., Kielkopf J. F., Stassun K. G., Hessman F. V., 2017, AJ, 153, 77
Dessart L., Hillier D. J., Woosley S., Livne E., Waldman R., Yoon S.-C., Langer N., 2016, MNRAS, 458, 1618
Djupvik A. A., Andersen J., 2010, Highlights of Spanish Astrophysics V. Springer, Berlin, Heidelberg, p. 211
Drout M. R. et al., 2016, ApJ, 821, 57
Ergon M. et al., 2014, A&A, 562, A17
Filippenko A. V., 1997, ARA&A, 35, 309
Filippenko A., 2000, AIP Conf. Proc., 522, 123
Folatelli G. et al., 2016, ApJ, 825, L22
Fremling C. et al., 2016, A&A, 593, A68
Georgy C., Ekström S., Meynet G., Massey P., Levesque E. M., Hirschi R., Eggenberger P., Maeder A., 2012, A&A, 542, A29
Gräfener G., Vink J. S., 2015, MNRAS, 455, 112
Groh J. H., Meynet G., Ekström S., 2013, A&A, 550, L7
Hachinger S., Mazzali P. A., Taubenberger S., Hillebrandt W., Nomoto K., Sauer D. N., 2012, MNRAS, 422, 70
Hamuy M. et al., 2009, ApJ, 703, 1612
Howell D. A.; Global Supernova Project, 2017, in American Astronomical Society Meeting Abstracts, Vol. 230, p. 318.03
Khatami D. K., Kasen D. N., 2019, ApJ, 878, 56
Lucy L. B., 1991, ApJ, 383, 308
Lyman J. D., Bersier D., James P. A., 2014, MNRAS, 437, 3848
Lyman J. D., Bersier D., James P. A., Mazzali P. A., Eldridge J. J., Fraser M., Pian E., 2016, MNRAS, 457, 328
Malesani D. et al., 2009, ApJ, 692, L84
Masci F. J. et al., 2019, PASP, 131, 018003
Mazzali P. A. et al., 2002, ApJ, 572, L61
Mazzali P. A. et al., 2008, Science, 321, 1185
Mazzali P. A., Deng J., Hamuy M., Nomoto K., 2009, ApJ, 703, 1624
Mazzali P. A., Walker E. S., Pian E., Tanaka M., Corsi A., Hattori T., Gal-Yam A., 2013, MNRAS, 432, 2463
Mazzali P. A., Sauer D. N., Pian E., Deng J., Prentice S., Ben Ami S., Taubenberger S., Nomoto K., 2017, MNRAS, 469, 2498
McCully C., Volgenau N. H., Harbeck D.-R., Lister T. A., Saunders E. S., Turner M. L., Siiverd R. J., Bowman M., 2018, in Guzman J. C., Ibsen J., eds, SPIE Astronomical Telescopes + Instrumentation, Vol. 10707, Software and Cyberinfrastructure for Astronomy V. SPIE, Bellingham, p. 141
Mould J. R. et al., 2000, ApJ, 529, 786
Nicholl M., 2018, Res. Notes AAS, 2, 230
Nomoto K., Suzuki T., Shlgeyama T., Kumagal S., Yamaokat H., Salo H., 1993, Nature, 364, 507
Nordin J., Brinnel V., Giomi M., Santen J. V., Gal-Yam A., Yaron O., Schulze S., 2020, Trans. Name Server Discovery Rep., 2020-511, 1
Pastorello A. et al., 2008, MNRAS, 389, 955
Piascik A. S., Steele I. A., Bates S. D., Mottram C. J., Smith R. J., Barnsley R. M., Bolton B., 2014, in Ramsay S. K., McLean I. S., Takami H., eds, SPIE Astronomical Telescopes + Instrumentation, Vol. 9147, Ground-based and Airborne Instrumentation for Astronomy V. SPIE, Bellingham, p. 2703
Piro A. L., 2015, ApJ, 808, L51
Podsiadlowski P., Joss P. C., Hsu J. J. L., 1992, ApJ, 391, 246
Poidevin F. et al., 2020, Trans. Name Ser. Class. Rep., 2020-571, 1
Poznanski D., Prochaska J. X., Bloom J. S., 2012, MNRAS, 426, 1465
Prentice S. J., Mazzali P. A., 2017, MNRAS, 469, 2672
Prentice S. J. et al., 2019, MNRAS, 485, 1559
Richmond M. W., Treffers R. R., Filippenko A. V., Paik Y., Leibundgut B., Schulman E., Cox C. V., 1994, AJ, 107, 1022
Richmond M. W., Treffers R. R., Filippenko A. V., Paik Y., 1996, AJ, 112, 732
Sahu D. K., Gurugubelli U. K., Anupama G. C., Nomoto K., 2011, MNRAS, 413, 2583
Sahu D. K., Anupama G. C., Chakradhari N. K., 2013, MNRAS, 433, 2
Sauer D. N., Mazzali P. A., Deng J., Valenti S., Nomoto K., Filippenko A. V., 2006, MNRAS, 369, 1939
Schlafly E. F., Finkbeiner D. P., 2011, ApJ, 737, 103
Shivvers I. et al., 2019, MNRAS, 482, 1545
Smartt S. J., 2009, ARA&A, 47, 63
Smartt S. J. et al., 2015, A&A, 579, A40
Smith N., Li W., Filippenko A. V., Chornock R., 2011, MNRAS, 412, 1522
Smith K. W. et al., 2019, Res. Notes Am. Astron. Soc., 3, 26
Smith K. W. et al., 2020, PASP, 132, 085002
Soker N., 2017, MNRAS, 470, L102
Sravan N., Marchant P., Kalogera V., 2019, ApJ, 885, 130
Stancliffe R. J., Eldridge J. J., 2009, MNRAS, 396, 1699
Steele I. A. et al., 2004, in Oschmann Jacobus M. J., ed., SPIE Conf. Ser. Vol. 5489, Ground-based Telescopes. SPIE, Bellingham, p. 679
Sukhbold T., Ertl T., Woosley S. E., Brown J. M., Janka H. T., 2016, ApJ, 821, 38
Suwa Y., Tominaga N., Maeda K., 2018, MNRAS, 483, 3607
Tanaka M. et al., 2009, ApJ, 692, 1131
Teffs J., Ertl T., Mazzali P., Hachinger S., Janka T., 2020, MNRAS, 492, 4369
Tonry J. L. et al., 2018, PASP, 130, 064505
Tsvetkov D. Y., Volkov I. M., Baklanov P., Blinnikov S., Tuchin O., 2009, Peremennye Zvezdy, 29, 2

Tsvetkov D. Y., Volkov I. M., Sorokina E. I., Blinnikov S. I., Pavlyuk N. N., Borisov G. V., 2012, Photometric Observations and Preliminary Modeling of Type iib Supernova 2011dh. preprint (arXiv:1207.2241)
Waxman E., Katz B., 2017, Handbook of Supernovae. Springer, Cham, p. 967
Wheeler J. C. et al., 1993, ApJ, 417, L71
Woosley S. E., Eastman R. G., Weaver T. A., Pinto P. A., 1994, ApJ, 429, 300
Woosley S. E., Langer N., Weaver T. A., 1995, ApJ, 448, 315
Woosley S., Sukhbold T., Kasen D., 2021, ApJ, 913, 145
Yaron O., Gal-Yam A., 2012, PASP, 124, 668

APPENDIX: PHOTOMETRIC OBSERVATIONS

See Tables A1 and A2.

Table A1. Apparent *BgVri* LCO Photomety of SN 2020cpg, no *k*-correction or extinction correction applied.

MJD_B	*B*(*err*) (mag)	$MJD_{g'}$	*g*'(*err*) (mag)	MJD_V	*V*(err) (mag)	$MJD_{r'}$	*r*'(err) (mag)	$MJD_{i'}$	*i*'(*err*) (mag)
58900.362	18.39(0.02)	58894.544	18.55(0.09)	58900.367	18.25(0.02)	58894.501	18.49(0.08)	58900.380	18.41(0.02)
58900.364	18.37(0.02)	58900.371	18.05(0.01)	58900.369	18.28(0.02)	58900.376	18.35(0.02)	58900.382	18.40(0.02)
58902.316	18.35(0.02)	58900.374	18.20(0.01)	58902.322	18.20(0.02)	58900.378	18.24(0.02)	58902.335	18.24(0.02)
58902.319	18.36(0.02)	58902.326	18.08(0.01)	58902.324	18.18(0.02)	58902.331	18.16(0.02)	58902.336	18.22(0.02)
58903.337	18.49(0.02)	58902.328	18.06(0.01)	58903.343	18.10(0.02)	58902.333	18.14(0.02)	58903.355	18.20(0.02)
58903.340	18.45(0.02)	58903.346	18.06(0.01)	58903.345	18.08(0.02)	58903.352	18.16(0.02)	58903.357	18.17(0.02)
58905.101	18.35(0.02)	58903.349	18.07(0.01)	58905.238	18.10(0.02)	58903.354	18.13(0.02)	58905.251	18.17(0.02)
58905.233	18.39(0.02)	58905.242	18.05(0.01)	58905.240	18.11(0.02)	58905.247	18.07(0.02)	58905.253	18.18(0.02)
58905.236	18.41(0.02)	58905.245	18.06(0.01)	58906.256	18.24(0.02)	58905.249	18.09(0.02)	58906.269	18.06(0.02)
58906.251	18.47(0.02)	58906.260	18.10(0.01)	58906.258	18.25(0.02)	58906.265	18.11(0.02)	58906.271	18.04(0.02)
58906.254	18.56(0.02)	58906.263	18.09(0.01)	58907.277	18.21(0.02)	58906.267	18.08(0.02)	58907.290	18.12(0.02)
58907.272	18.59(0.02)	58907.281	18.14(0.01)	58907.279	18.24(0.02)	58907.286	18.02(0.02)	58907.291	18.06(0.02)
58907.274	18.58(0.02)	58907.283	18.16(0.01)	58909.253	18.35(0.02)	58907.288	18.05(0.02)	58909.265	18.08(0.02)
58909.248	18.63(0.02)	58909.256	18.16(0.02)	58909.255	18.37(0.02)	58909.262	18.01(0.02)	58909.267	18.03(0.02)
58909.250	18.73(0.02)	58909.259	18.17(0.02)	58910.336	18.09(0.02)	58909.264	18.04(0.02)	58910.349	18.01(0.02)
58910.331	18.48(0.02)	58910.340	18.29(0.02)	58910.338	18.06(0.02)	58910.345	18.07(0.02)	58910.350	18.06(0.02)
58910.333	18.52(0.02)	58910.342	18.23(0.02)	58912.105	18.18(0.02)	58910.347	18.10(0.02)	58912.118	18.05(0.04)
58912.100	18.77(0.02)	58912.109	18.37(0.02)	58912.107	18.34(0.02)	58912.114	18.11(0.02)	58912.119	18.06(0.04)
58912.102	18.78(0.02)	58912.111	18.39(0.02)	58914.389	18.45(0.02)	58912.116	18.09(0.02)	58914.401	18.09(0.03)
58914.383	19.01(0.02)	58914.392	18.63(0.02)	58914.390	18.44(0.02)	58914.397	18.17(0.02)	58914.403	18.14(0.03)
58914.386	19.10(0.02)	58914.395	18.55(0.02)	58916.355	18.76(0.02)	58914.399	18.18(0.02)	58916.368	18.19(0.02)
58916.350	19.38(0.04)	58916.359	18.80(0.02)	58916.357	18.70(0.02)	58916.364	18.20(0.02)	58916.369	18.22(0.02)
58916.352	19.37(0.04)	58916.361	18.80(0.02)	58917.323	18.48(0.02)	58916.366	18.28(0.02)	58917.347	18.37(0.05)
58917.313	19.31(0.05)	58917.331	18.89(0.02)	58917.327	18.56(0.02)	58917.341	18.28(0.02)	58917.349	18.49(0.05)
58917.318	19.24(0.05)	58917.336	18.98(0.02)	58920.620	18.62(0.06)	58917.344	18.34(0.02)	58920.643	18.46(0.05)
58920.610	19.47(0.09)	58920.627	19.24(0.02)	58920.623	18.71(0.06)	58920.638	18.54(0.02)	58920.646	18.40(0.05)
58920.615	19.47(0.09)	58920.632	19.14(0.02)	58924.184	18.87(0.04)	58920.640	18.50(0.02)	58924.208	18.40(0.03)
58924.174	19.94(0.06)	58924.192	19.45(0.02)	58924.188	18.85(0.04)	58924.202	18.59(0.02)	58924.210	18.40(0.03)
58924.179	19.90(0.06)	58924.197	19.57(0.02)	58927.094	19.09(0.04)	58924.205	18.60(0.02)	58927.118	18.59(0.02)
58927.084	20.25(0.06)	58927.102	19.75(0.02)	58927.098	19.00(0.04)	58927.112	18.81(0.02)	58927.120	18.62(0.02)
58927.089	20.19(0.06)	58927.107	19.67(0.02)	58931.054	19.37(0.04)	58927.115	18.85(0.02)	58931.080	18.81(0.01)
58931.044	20.65(0.05)	58931.062	20.11(0.02)	58931.058	19.52(0.04)	58931.072	19.09(0.02)	58931.084	18.78(0.01)
58931.049	20.42(0.05)	58931.067	20.05(0.02)	58949.708	19.92(0.12)	58931.076	19.15(0.02)	58939.657	19.12(0.01)
–	–	–	–	58951.685	19.99(0.08)	58939.653	19.34(0.02)	58951.692	19.53(0.03)
–	–	–	–	58959.235	20.11(0.05)	58951.689	19.66(0.04)	58959.243	19.54(0.04)
–	–	–	–	58974.207	20.20(0.15)	58959.239	19.77(0.03)	58974.215	19.76(0.11)
–	–	–	–	58982.144	20.48(0.15)	58974.211	20.01(0.10)	58982.151	19.88(0.05)
–	–	–	–	58985.538	20.53(0.07)	58982.147	20.03(0.04)	58985.546	19.91(0.05)
–	–	–	–	58993.431	20.36(0.09)	58985.542	20.07(0.03)	58993.439	20.14(0.09)
–	–	–	–	59000.823	20.67(0.14)	58993.435	20.17(0.11)	59000.831	20.43(0.15)
–	–	–	–	59008.891	20.54(0.15)	59000.827	20.21(0.10)	59008.898	20.17(0.06)
–	–	–	–	–	–	59008.894	20.40(0.12)	–	–

Table A2. Apparent *c*+*o* band ATLAS photometry for SN 2020cpg. Photometry has not been corrected for either extinction or *k*-correction.

MJD_c	*c*(err) (mag)	MJD_o	*o*(err) (mag)	MJD_o	*o*(err) (mag)
58903.464	18.10(0.06)	58901.489	18.33(0.08)	58953.488	19.32(0.17)
58903.499	18.10(0.05)	58901.493	18.23(0.07)	58957.400	19.80(0.30)
58903.503	18.19(0.06)	58901.500	18.24(0.06)	58957.412	19.59(0.20)
58903.512	18.18(0.05)	58901.511	18.22(0.06)	58957.415	19.87(0.27)
58911.503	18.13(0.05)	58905.562	18.07(0.05)	58961.441	19.38(0.16)
58931.502	19.27(0.13)	58905.565	18.09(0.05)	58961.444	19.78(0.22)
58931.522	19.59(0.17)	58905.573	18.06(0.05)	58961.465	19.67(0.21)
58931.530	19.45(0.15)	58905.583	18.10(0.05)	58965.446	19.26(0.20)
58931.539	19.46(0.16)	58913.454	18.20(0.07)	58965.457	19.73(0.29)
58935.583	19.78(0.25)	58913.458	18.10(0.06)	58965.491	19.55(0.21)
58935.586	19.55(0.21)	58913.463	18.24(0.07)	58969.404	20.12(0.30)
58959.426	20.14(0.30)	58913.477	18.19(0.07)	58969.417	19.83(0.23)
58959.430	19.66(0.19)	58917.449	18.25(0.18)	58969.421	20.02(0.27)
58959.438	20.18(0.28)	58917.457	18.32(0.19)	58969.428	19.75(0.22)
58959.455	20.05(0.27)	58917.467	18.78(0.27)	58971.423	19.68(0.26)
58967.415	19.96(0.23)	58925.533	18.70(0.21)	58971.439	19.54(0.25)
58967.425	20.10(0.26)	58925.538	18.65(0.17)	58977.446	19.21(0.28)
58967.460	20.10(0.28)	58933.537	19.36(0.18)	58981.387	19.63(0.20)
58982.391	20.06(0.25)	58933.543	19.02(0.13)	58981.404	20.07(0.30)
58987.399	20.12(0.27)	58933.547	19.14(0.15)	58981.415	19.76(0.26)
–	–	58933.559	18.86(0.12)	58985.366	19.94(0.23)
–	–	58937.496	19.27(0.13)	58985.380	20.12(0.28)
–	–	58937.498	19.32(0.12)	58989.354	19.76(0.18)
–	–	58937.508	18.99(0.29)	58989.358	20.08(0.25)
–	–	58937.522	19.47(0.17)	58989.393	20.06(0.24)
–	–	58941.433	18.80(0.13)	58997.324	20.07(0.28)
–	–	58941.445	18.91(0.15)	58997.331	20.13(0.28)
–	–	58941.448	19.50(0.24)	58997.335	20.06(0.30)
–	–	58941.463	19.18(0.27)	58999.352	19.83(0.28)
–	–	58943.479	19.44(0.25)	58999.355	19.77(0.29)
–	–	58943.484	19.47(0.30)	59006.346	19.44(0.30)
–	–	58949.477	19.20(0.26)	59013.351	20.26(0.30)
–	–	58949.482	19.30(0.30)	59013.357	20.25(0.29)
–	–	58951.461	18.89(0.28)	59013.367	20.23(0.28)
–	–	58951.469	19.57(0.29)	59021.328	20.08(0.27)
–	–	58951.482	19.17(0.29)	59021.346	20.04(0.27)
–	–	58953.467	19.28(0.19)	59025.321	20.26(0.30)
–	–	58953.474	19.92(0.28)	59029.318	19.44(0.30)
–	–	58953.478	19.46(0.19)	59037.297	19.95(0.29)

This paper has been typeset from a TEX/LATEX file prepared by the author.